An Analysis of the Origin and Propagation of the Multiple Coronal Mass Ejections of 2010 August 1

Harrison, R. A.; Davies, J. A.; Möstl, C.; Liu, Y.; Temmer, M.; Bisi, M. M.; Eastwood, J. P.; de Koning, C. A.; Nitta, N.; Rollett, T.; Farrugia, C. J.; Forsyth, R. J.; Jackson, B. V.; Jensen, E. A.; Kilpua, E. K. J.; Odstrcil, D.; Webb, D. F.

AN ANALYSIS OF THE ORIGIN AND PROPAGATION OF THE MULTIPLE CORONAL MASS EJECTIONS OF 2010 AUGUST 1

R. A. HARRISON[1], J. A. DAVIES[1], C. MÖSTL[2,3,4], Y. LIU[4,5], M. TEMMER[2,3], M. M. BISI[6,7], J. P. EASTWOOD[8],
C. A. DE KONING[9], N. NITTA[10], T. ROLLETT[2,3], C. J. FARRUGIA[11], R. J. FORSYTH[8], B. V. JACKSON[7],
E. A. JENSEN[12], E. K. J. KILPUA[13], D. ODSTRCIL[14], AND D. F. WEBB[15]

[1] RAL Space, Rutherford Appleton Laboratory, Harwell Oxford, Didcot OX11 0QX, UK; Richard.Harrison@stfc.ac.uk
[2] Institute of Physics, University of Graz, Graz A-8010, Austria
[3] Space Research Institute, Austrian Academy of Sciences, Graz A-8042, Austria
[4] Space Sciences Laboratory, University of California, Berkeley, CA 94720, USA
[5] State Key Laboratory of Space Weather, National Space Science Center, Chinese Academy of Sciences, Beijing, China
[6] Institute of Mathematics and Physics, Aberystwyth University, Ceredigion SY23 3BZ, UK
[7] Center for Astrophysics and Space Sciences, University of California, San Diego, La Jolla, CA 92093-0424, USA
[8] The Blackett Laboratory, Imperial College London, London SW7 2AZ, UK
[9] NOAA Space Weather Prediction Center, Boulder Colorado, CO 80305, USA
[10] Solar and Astrophysics Laboratory, Lockheed Martin Advanced Technology Centre, Palo Alto, CA 94304-1191, USA
[11] Space Science Center and Department of Physics, University of New Hampshire, Durham, NH 03824, USA
[12] Planetary Science Institute, 1700 East Fort Lowell, Suite 106, Tucson, AZ 85719-2395, USA
[13] Department of Physics, University of Helsinki, P.O. Box 64, FI-00014 Helsinki, Finland
[14] Department of Computational and Data Sciences, George Mason University/NASA Goddard Space Flight Center, Mail Code 674, Greenbelt, MD 20771, USA
[15] Institute for Scientific Research, Boston College, 885 Center Street, Newton, MA 02459, USA

ABSTRACT

On 2010 August 1, the northern solar hemisphere underwent significant activity that involved a complex set of active regions near central meridian with, nearby, two large prominences and other more distant active regions. This activity culminated in the eruption of four major coronal mass ejections (CMEs), effects of which were detected at Earth and other solar system bodies. Recognizing the unprecedented wealth of data from the wide range of spacecraft that were available—providing the potential for us to explore methods for CME identification and tracking, and to assess issues regarding onset and planetary impact—we present a comprehensive analysis of this sequence of CMEs. We show that, for three of the four major CMEs, onset is associated with prominence eruption, while the remaining CME appears to be closely associated with a flare. Using instrumentation on board the *Solar Terrestrial Relations Observatory* spacecraft, three of the CMEs could be tracked out to elongations beyond $50°$; their directions and speeds have been determined by various methods, not least to assess their potential for Earth impact. The analysis techniques that can be applied to the other CME, the first to erupt, are more limited since that CME was obscured by the subsequent, much faster event before it had propagated far from the Sun; we discuss the speculation that these two CMEs interact. The consistency of the results, derived from the wide variety of methods applied to such an extraordinarily complete data set, has allowed us to converge on robust interpretations of the CME onsets and their arrivals at 1 AU.

Key words: solar–terrestrial relations – Sun: corona – Sun: coronal mass ejections (CMEs) – Sun: filaments, prominences – Sun: flares – Sun: heliosphere

1. INTRODUCTION

On 2010 August 1, a series of coronal mass ejections (CMEs) were launched in quick succession, originating from an extended and complex region of coronal activity on the northern hemisphere of the Earth-facing solar disk. By exploiting observations from the wide range of spacecraft that were operational during this interval, we are able to perform a comprehensive analysis, and hence advance our understanding, of various aspects of CME onset and propagation. In particular, we investigate the association of these CMEs with surface phenomena—such as flares and prominence channels—and assess the potential for planetary impact, particularly at Earth. Moreover, the data reveal the fortuitous, albeit complicating, observation of an apparent CME–CME interaction. The results of this study feed into mounting worldwide effort to apply such understanding of CME onset and propagation to issues of space weather.

Following the deep and extended solar minimum of 2007–2009, there was much interest in the first signs of the in-

creasing activity of the new cycle, especially with the advent of high-resolution observations of the extreme-ultraviolet (EUV) corona from the recently launched NASA *Solar Dynamics Observatory* (*SDO*) spacecraft. Prior to 2010 August, a number of high-latitude active regions had been developing, but the interval around August 1 represented a spectacular increase in terms of such activity and its associated magnetic complexity. This involved a number of prominence eruptions, a series of small flares, and quite rapid magnetic development that appears to have involved regions on the solar surface separated by many tens of degrees. The *SDO* observations, as well as the underlying magnetic configuration derived therefrom, are presented by Schrijver & Title (2011).

The analysis documented here concentrates on the identification, propagation, and evolution of the associated CMEs, as they travel from the low solar corona through the inner heliosphere out to distances beyond 1 Astronomical Unit (1 AU). We present and interpret data from a number of instruments, making, in particular, coronal and heliospheric observations of these
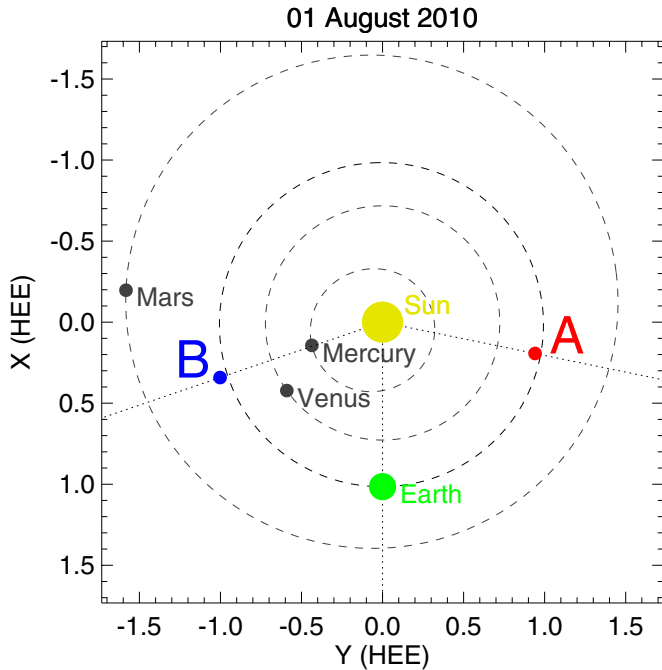
01 August 2010

Figure 1. Locations of the *STEREO-A* and *STEREO-B* spacecraft, and the inner planets (Mercury, Venus, Earth, and Mars) in the Heliocentric Earth Ecliptic (HEE) *X–Y* plane on 2010 August 1 (see "Where is *STEREO*?" Web tool: http://stereo-ssc.nascom.nasa.gov/where/).

CMEs, as well as applying a variety of techniques, to achieve a consistent picture of the event sequence. Moreover, we link our interpretation to (1) the *SDO* analysis of features at the Sun (Schrijver & Title 2011) to investigate the onset processes, (2) observations at the Earth and at other solar system locations (C. Möstl et al. 2012, in preparation) to study potential planetary impact, (3) various issues pertaining to CME–CME interaction (Liu et al. 2012; Martinez Oliveros et al. 2012; Temmer et al. 2012), and (4) results from MHD simulations of the inner heliosphere (D. Odstrcil et al. 2012, in preparation). Furthermore, Webb et al. (2012) are endeavouring to assemble a view of the CMEs from a truly global perspective. Thus, the current work should be regarded as a component of a wider, strategic study.

Much of the analysis presented in this paper is based on imaging observations from the Sun Earth Connection Coronal and Heliospheric Investigation (SECCHI; Howard et al. 2008) on NASA's twin *Solar Terrestrial Relations Observatory* (*STEREO*; Kaiser et al. 2008). The SECCHI package on each *STEREO* spacecraft comprises an EUV Imager (EUVI), two coronagraphs (COR1 and COR2), and the Heliospheric Imager (HI) instrument, which consists of two cameras, HI-1 and HI-2. Between them, the SECCHI instruments can image the chromosphere, corona, and inner heliosphere out to distances well beyond 1 AU. With both of the *STEREO* spacecraft being situated more than 70° from the Sun–Earth line at the time (*STEREO-A* was 78°.3 west and *STEREO-B* was 71°.2 east of Earth on 2010 August 1, as illustrated in Figure 1), the complex near-Earth bound sequence of CMEs could be imaged propagating out to 1 AU, which is highly conducive to accurately determining the CME kinematics. We also include an analysis of CME-associated type II radio bursts detected by the *STEREO*/WAVES instruments (*S*/WAVES; Bougeret et al. 2008) and of heliospheric imaging observations made by

the Solar Mass Ejection Imager (SMEI; Eyles et al. 2003; Jackson et al. 2004) on the *Coriolis* spacecraft from a near-Earth vantage point. Finally, we present a brief analysis of in situ measurements, showing the subsequent arrival of the CMEs at Earth on August 3/4, made by the near-Earth *Wind* spacecraft (Acũna et al. 1995).

This paper has important implications in terms of space weather predictions. The most pronounced signature in the integrated 1–8 Å X-ray flux, provided by the geostationary *GOES* spacecraft, during this interval was only classified as a C3 event, and only one weak halo CME, listed as a "poor event," was identified from coronagraph observations taken by the LASCO/C3 instrument on the *Solar and Heliospheric Observatory* spacecraft (Brueckner et al. 1995); these are traditionally used tools for monitoring space weather conditions. We do note, however, that LASCO experienced several data gaps on August 1, which may have hindered the identification of CMEs. That said, these observations belie the true nature of the CMEs of that period, not least because views from a position significantly away from the Sun–Earth line are particularly advantageous for identifying and characterizing such Earth-directed events.

2. OBSERVATIONS

2.1. An Overview of the STEREO Heliospheric Imager Observations

Initially, we summarize the observations of this series of CMEs that were made by the *STEREO*/SECCHI/HI instruments (Harrison et al. 2008; Eyles et al. 2009), which arguably provide the most complete introduction to the sequence of events. The HI instrument on each of the pair of *STEREO* spacecraft comprises two wide-angle, visible-light camera systems, HI-1 and HI-2, which we denote as HI-1A and HI-2A for *STEREO-A* and HI-1B and HI-2B for *STEREO-B*. The boresight of the 20° square HI-1 field of view is nominally aligned in the ecliptic plane at an elongation of 14°. Similarly, the 70° wide HI-2 field of view is centered on the ecliptic, but at an elongation of 53°.7. During the phase of the mission when the observations presented in this paper were taken, the *STEREO*/HI instruments were able to view the Sun–Earth line from two widely spaced vantage points, enabling a unique view of Earth-directed events.

A selection of images from HI-1 on *STEREO-A*, covering an interval extending from 05:29 to 22:09 UT on 2010 August 1, are presented in Figure 2. The specific images presented are chosen to illustrate the salient features of the CME sequence. Note the 40 minute cadence of HI-1 during such nominal operations. The HI-1A images shown in the upper six panels of Figure 2 have undergone subtraction of a daily background; this removes the contribution of the F-corona and the more slowly varying components of the K-corona. The lower six panels present corresponding difference images, where each image has had the previous image subtracted. In such difference imaging, light gray/white regions reveal an increase in intensity (indicating an enhanced plasma density) relative to the time of the previous image, whereas dark gray/black regions show a reduction in intensity (density). This approach highlights faint propagating plasma features. Contours of elongation, separated by 5°, are overlaid on the first background-subtracted and difference images shown. Venus and Mercury are visible at around 10° and 20° elongation, respectively, and the Sun (centered at 0° elongation) is just off the center right of each image.
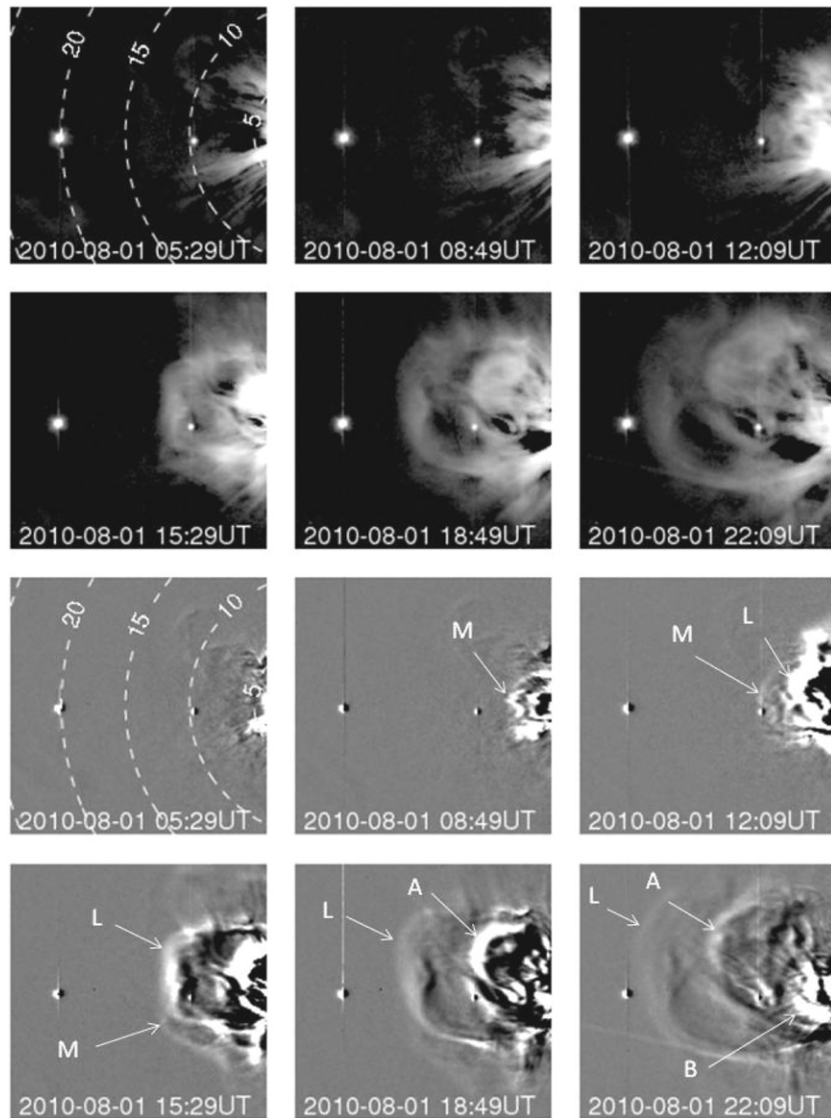
Figure 2. Six selected HI-1A images from 2010 August 1 in each of two formats, background-subtracted (upper six panels) and difference (lower six panels). Times are given on each panel. Elongation angle contours are overlaid on the first image of each format. Signatures of Venus and Mercury (at 10° and 20° elongation, respectively) are evident in each image, and the Sun (centered at 0° elongation) is just off the center right of each image. CMEs L, M, A and B are identified on the difference images.

The sequence of events revealed by these images is as follows:

1. The first frames of the interval show the ascent into the HI-1A field of view of a double-loop CME, with each loop exhibiting a characteristic, sideways-oriented m-shape. Because of its shape, we label this CME as M. The initial loop of CME M first enters the HI-1A field of view at around 05:29 UT, with the second near-identical loop trailing by about an hour. The double-m shaped structure of M is most apparent in the 08:49 UT difference image (lower portion of Figure 2).

2. At around 09:29 UT, a second CME (which we label as L) enters the HI-1A field of view. L is a bright but rather irregular loop-like CME that, like M, is centered on the ecliptic plane. In the panel at 12:09 UT, CME M is still clearly discernable at larger elongations than L (especially in the difference image; lower portion of the figure). However, by 15:29 UT, CME L totally obscures M. Whether the two CMEs physically interact or simply pass in front of/behind each other depends, of course, on their relative propagation directions; we discuss this in more detail later. Having said that, it is impossible to distinguish any features that are easily attributable to CME M later in the sequence, leading to the suggestion that there was indeed a significant interaction.

3. The images at 15:29 and 18:49 UT reveal another loop-like CME following L, clearly identifiable in both the difference and background-subtracted images. Unlike L and M, this CME, which we label as A, propagates along a direction somewhat north of the ecliptic plane. CME A first enters the HI-1A field of view at about 13:29 UT.

4. In the 22:09 UT image, and particularly the difference image (lower portion of the figure), a bright irregular-shaped CME can be seen following A. It enters the HI-1A field of view at 20:09 UT. We label this event CME B. B propagates along a roughly ecliptic oriented trajectory, well into the HI-1A field of view, while the northward-bound CME, A, is still clearly visible at larger elongations. By this time, the now faint outer loop of CME L is approaching the 20° elongation of Venus.
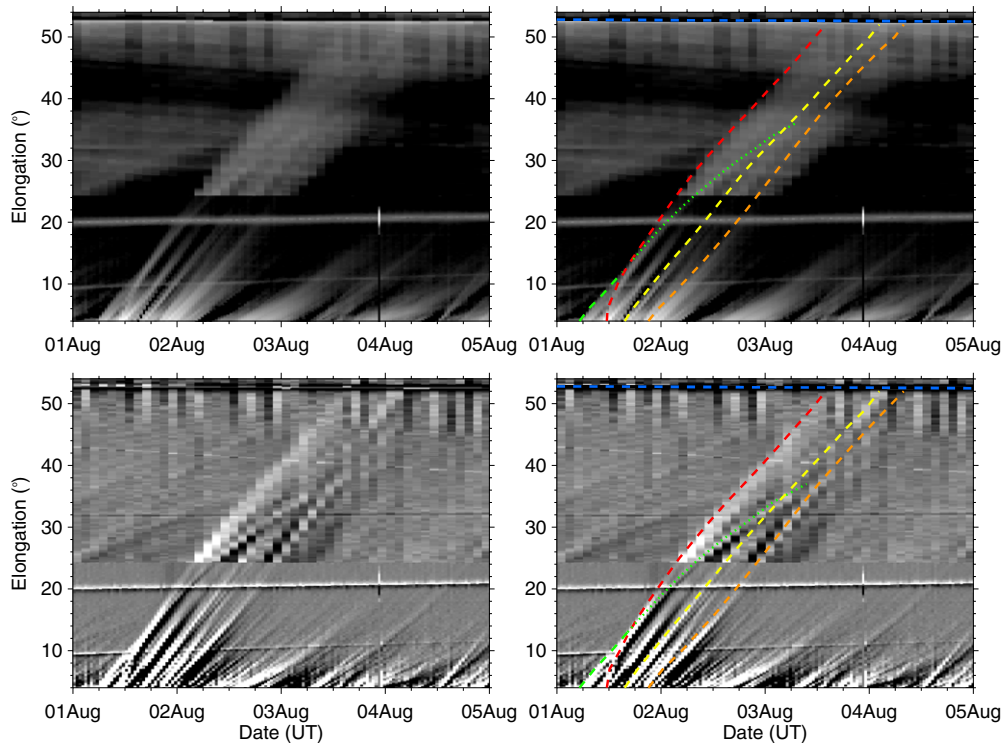
Figure 3. Time–elongation maps (J-maps) covering the interval 2010 August 1 to 5, constructed from HI-1A and HI-2A background-subtracted (upper panels) and difference (lower panels) observations extending from 4° to 54° elongation along the ecliptic. HI-1A data are plotted out to 24° elongation, HI-2A data therefrom. Right-hand panels show tracks corresponding to CMEs M, L, A, and B (marked in green, red, yellow, and orange, respectively). Near-horizontal signatures of Mercury, Venus, and Earth can be seen at elongations of 10°, 20°, and 53°, respectively; the latter is marked by a dashed blue line.

The above description is based on observations from the HI-1 instrument on *STEREO-A* on 2010 August 1, which, as noted earlier, was 78°.3 west of the Sun–Earth line at the time. The view from HI on *STEREO-B* (71°.2 east of Earth) is essentially a reflection of that from *STEREO-A*, and thus HI-1B would be expected to provide an equally impressive view of this sequence of near-Earth-directed CMEs. However, *STEREO-B* experienced an extensive data gap, lasting from approximately 10:00 UT on August 1 until 04:00 UT on August 2. Thus, we have a limited coverage from HI-1B, corresponding to only the start of the interval of interest. While these early images do show CME M propagating through the near-Sun portion of the field of view of HI-1B, there is little coverage of the majority of the passage of CMEs L, A, and B through the HI-1B field of view.

2.2. Deriving the Kinematics of Each CME

One of the principal aims of this paper is to ascertain the radial speed and direction of propagation for each of the CMEs in this sequence, to assess such issues as the possibility of CME–CME interaction and planetary impact. Particularly since the advent of wide-angle imaging of the inner heliosphere, a number of techniques have been developed to investigate the three-dimensional kinematics of solar transients from their signatures in imaging observations. In this paper, we concentrate extensively, but not exclusively, on methods of deriving the propagation characteristics of the CMEs based on the analysis of their time-elongation profiles (e.g. Rouillard et al. 2008; Lugaz 2010; Liu et al. 2010a). Such time-elongation profiles are often extracted manually from time-elongation maps, commonly called J-maps, derived from coronal/heliospheric imaging observations made along a fixed solar radial. The use of J-maps, created in that case using coro-

nagraph observations from LASCO, was pioneered by Sheeley et al. (1999); the J-mapping technique has since been developed for use with heliospheric imaging data from HI and SMEI (e.g., Rouillard et al. 2008; Sheeley et al. 2008; Davies et al. 2009). In such J-maps, the signatures of anti-sunward-propagating solar transients are evident as positively inclined traces.

Figure 3 presents J-maps derived from both background-subtracted (upper two panels) and difference images (lower two panels) taken by the HI-1 and HI-2 cameras on *STEREO-A* and constructed along a position angle (P.A.) of 85°.2. This P.A. was used as it corresponds to that of the Earth (the ecliptic) as viewed from *STEREO-A* at the time of the observations (the Earth being at a latitude of some 5°.8 north of the solar equator). Note that P.A.s are measured counterclockwise from solar equatorial north, and that the P.A. of Earth was 277°.0 as viewed from *STEREO-B* at the time. The *STEREO-A* J-maps presented in Figure 3 extend from 00:00 UT on August 1 to 00:00 UT on August 5, encompassing the passage of the series of four major CMEs launched on August 1 through the HI field of view, and range from 4° to 54° in elongation (i.e., extending just beyond the elongation of Earth that was 53° as viewed from *STEREO-A* at this time). In these J-maps, observations from the HI-1 camera are plotted in the 19°–24° elongation range, where, in nominal operations, the ecliptic portions of the HI-1 and HI-2 fields of view overlap. The panels on the right-hand side of Figure 3 reproduce the left-hand panels but with the addition of colored dashed/dotted curves indicating, as a guide, the tracks corresponding to the four CMEs identified above (M: green; L: red; A: yellow; B: orange) and a blue dashed horizontal line indicating the elongation of Earth. The near-horizontal signatures of Venus and Mercury can be identified in each panel at around 10° and 20° elongation, respectively.
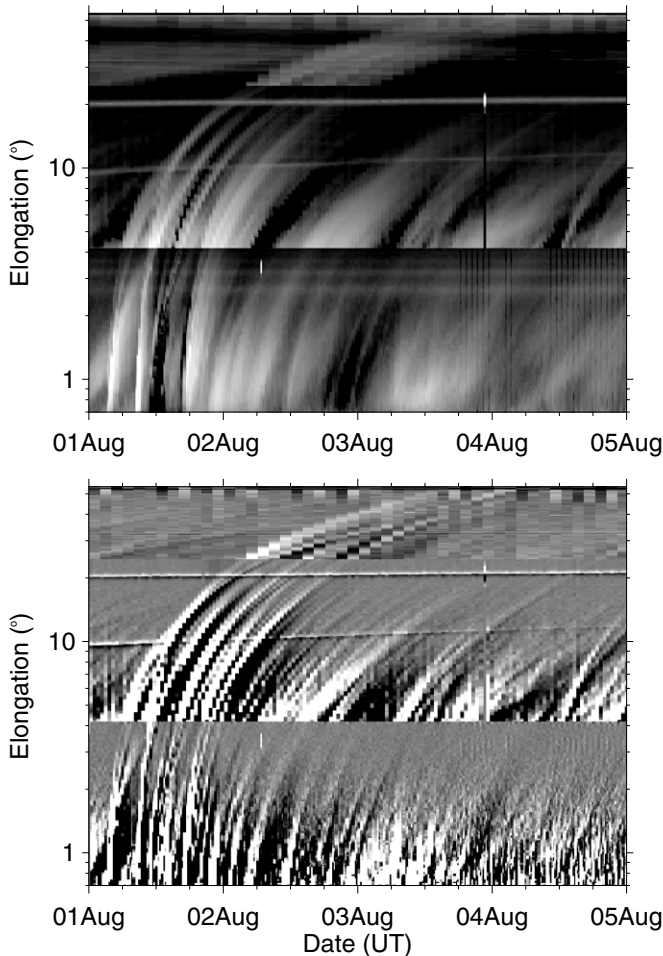
Figure 4. Background-subtracted (top panel) and difference (bottom panel) J-maps, like those in Figure 3, but with the addition of ecliptic COR2 coronagraph observations at elongations below around 4°. In this case, the elongation axis is plotted on a logarithmic scale.

The complexity of the set of time-elongation tracks corresponding to the propagation of the August 1 CMEs along the ecliptic is immediately obvious. However, it is evident that some of the tracks extend to elongations of at least 50°, i.e., out to distances near 1 AU for Earthward-directed CMEs. In Figure 4, we reproduce the background-subtracted (upper panel) and difference J-maps (lower panel) but with the addition of ecliptic coronagraph observations from *STEREO*/COR2 at elongations from 0°7 to somewhat in excess of 4°. In the slight overlap region between the fields of view of COR2 and HI-1, data from the former are plotted. In order that observations from the COR2 instrument, with its smaller field of view, are more clearly visible, elongation is plotted on a logarithmic scale.

The first clear track that we see in Figures 3 and 4 corresponds to CME M (Figure 3; green dashed line). The track of the subsequently launched CME L (Figure 3; red dashed line) catches up with that of M at an elongation of around 12°; this confirms what is revealed by the images (Figure 2). Whether there is any actual physical interaction between the two CMEs, with M perhaps being swept up by L, depends critically on their relative propagation directions. Although the track of M is illustrated as continuing to elongations beyond this "interaction region" (Figure 3; green dotted line), it is not possible, using either the J-maps or the images, to unambiguously distinguish any signatures that can clearly be attributed to CME M later in

the interval. In fact, close inspection of the HI-1 images suggests that this apparent extension of M's track actually corresponds to structure within the trailing edge of CME L. The lack of any evidence for the continued existence (in its previous form) of CME M after it has been obscured by CME L lends credence to the suggestion of CME–CME interaction. Indeed, Temmer et al. (2012), who perform an analysis of this very issue based on several techniques for discerning CME propagation direction, conclude that there is a real interaction between M and L. We discuss the relevance of any of our results to this point as they arise. In light of this discussion, we make no use of that part of the time-elongation profile of M at elongations above 15°. The tracks of CMEs L and A, and less clearly B, cross the elongation of Earth. Although this does not, of course, necessarily imply passage over the Earth itself, but may again be a line-of-sight effect, the following analysis does confirm that these CMEs were near-Earth-directed.

Having established the CMEs observed by HI during this interval and identified their signatures in ecliptic J-maps, we embark on an analysis to determine, from their time-elongation profiles mainly derived from *STEREO*/HI data, the following information for each: (1) radial speed and direction; (2) projected onset time and location; and (3) potential for Earth impact, and if Earth impact is anticipated, the projected arrival time of the CME at Earth. In the following sections, we present an analysis of each of the principal CME structures. Our aim is not only to piece together the events of August 1, but also to explore what methods are open to us in doing such an analysis.

2.2.1. CME M

The double m-shaped CME, M, was imaged by HI-1A and also, very early on in its propagation (prior to 09:30 UT on August 1), by HI-1B. M cannot be unambiguously identified as a distinct feature after around 15:29 UT, so its time-elongation profile even from *STEREO-A* is limited to a maximum elongation of 15°. Two of the principal techniques that can be used to derive solar transient kinematics from their time-elongation profiles (Fixed Phi Fitting, FPF, Rouillard et al. 2008; Harmonic Mean Fitting, HMF, Lugaz 2010) require observations from only a single vantage point; these techniques will be discussed in more detail with reference to the analysis of CME L below. However, to produce accurate results, these methods require the extent of the time-elongation profile to be significantly longer than is available for CME M (see Möstl et al. 2011, and references therein), so their use is considered inappropriate in this case.

Thus, to ascertain the propagation characteristics of CME M, we apply the triangulation method developed by Liu et al. (2010a, 2010b), based on the use of simultaneous time-elongation profiles extracted from *STEREO-A* and *STEREO-B* J-maps constructed along the ecliptic using COR2 and HI-1 observations. Whereas the single spacecraft analysis techniques mentioned above produce a single estimate of radial speed and propagation direction over the entire transient trajectory, which both have to be roughly constant for the analysis to produce valid results, these constraints are removed by use of a triangulation approach. In this case, of course, results from the triangulation technique, which requires simultaneous observations from both spacecraft, are limited to that time prior to the *STEREO-B* data gap. C. Möstl et al. (2012, in preparation) and Liu et al. (2010b) provide summaries of the relative advantages and disadvantages of the various methods of deriving solar transient kinematics.
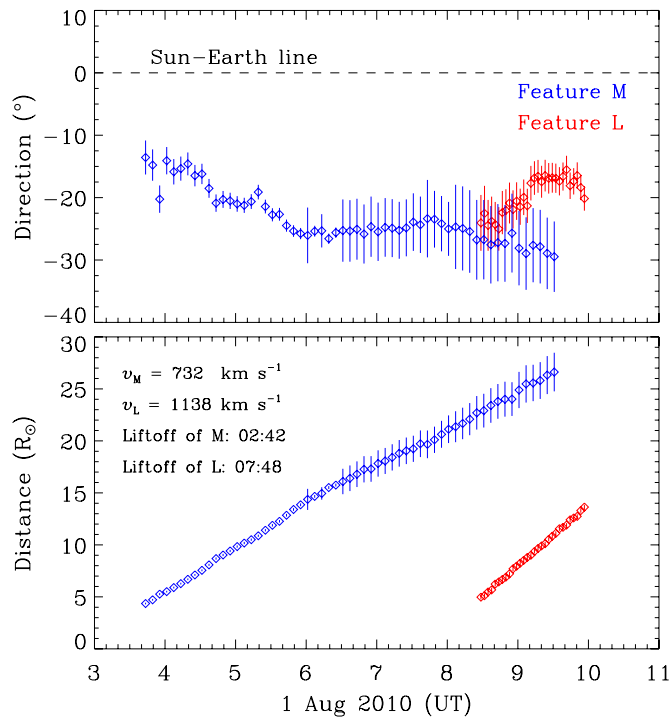
Figure 5. Times series of propagation direction (top panel) and radial distance (bottom panel) for CME M (blue) and CME L (red) derived from triangulation analysis of ecliptic COR2 and HI-1 observations made, simultaneously, by the two *STEREO* spacecraft, following the method of Liu et al. (2010a, 2010b). Estimates of radial speeds and onset times, for each of the two CMEs, are quoted on the bottom panel.
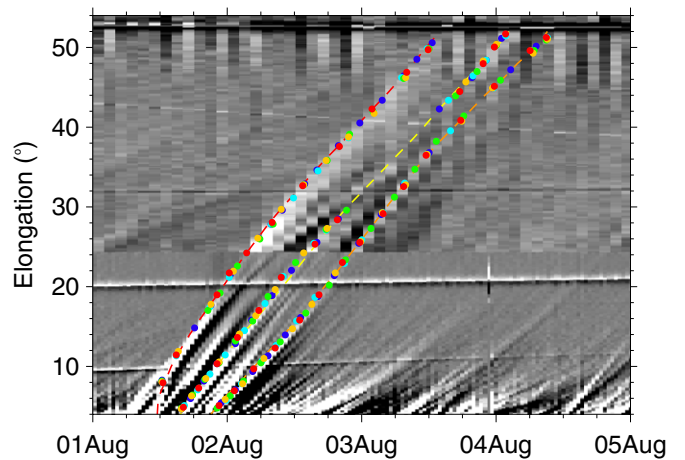

Figure 6. *STEREO-A*/HI difference J-map, identical to that shown in the lower panels of Figure 3, with curves indicating the tracks corresponding to CMEs L, A, and B (red, yellow, and orange dashed lines, respectively). For each of the three CMEs, five sets of manually selected points tracing the CME front are overlaid (each set of points is plotted in a different color).

The results of the triangulation analysis, following the method of Liu et al. (2010a, 2010b), are presented in Figure 5. Figure 5 presents time series of the propagation direction (upper panel) and radial distance (lower panel) of CME M in blue. Results for CME L, shown in red and derived from COR2 data only due to the onset of the *STEREO-B* data gap, are discussed later. As the time-elongation profiles used in the analysis are derived from ecliptic observations, the propagation direction equates to an ecliptic longitude with positive/negative directions denoting propagation west/east of the Sun–Earth line. The triangulation technique also enables the computation of a corresponding time series of the radial speed (not shown). The radial speeds exhibit significant scatter as the calculation of the speed, which is derived from the rate of change of adjacent radial distance estimates, magnifies small fluctuations in the latter. However, the triangulation suggests an average value of 732 km s^{-1} for CME M, at least during this early phase of its propagation. The technique also indicates an eastward rotation in CME propagation longitude from an initial value of E12° (i.e., 12° east of the Sun–Earth line) to a near constant value of around E30° (see upper panel of Figure 5, blue symbols). It should be remembered that these results are derived from a combination of COR2 and HI-1 observations from both *STEREO-A* and *STEREO-B* and thus only cover the interval 03:30 to 09:30 UT on August 1. The back-projected onset time for M, assuming a constant velocity of 732 km s^{-1}, is 02:42 UT on that day.

2.2.2. CME L

The clear trace produced by CME L in the *STEREO-A* ecliptic J-maps (Figures 3 and 4) can be continuously tracked out to at

least 50° (dashed red line in the right-hand panels of Figure 3). Figure 6 reproduces the difference HI J-map shown in the lower panels of Figure 3, with three curves indicating the tracks corresponding to CMEs L, A, and B (red, yellow, and orange dashed lines, respectively). For each of the three CMEs, five sets of manually selected points tracing the CME front are overlaid (each set of points is plotted in a different color). Note that each CME front is traced five times (using difference J-maps) to evaluate the random errors inherent in manually tracking such a feature; subsequent averaging of the derived parameters enables their random error to be reduced. Of course, any systematic errors resulting from, for example, the misidentification of a track are not so easily mitigated. In this section, we consider the track made by CME L. Due to the highly complex nature of the near-Sun coronal region, we avoid selecting points along CME L at elongations below around 7°.5, and care has also been taken when selecting points between some 10° and 15° elongation where the tracks of CMEs M and L overlap.

Having determined the time-elongation profile of CME L by manual tracking, we apply two often-used techniques for deriving the kinematic properties of a solar transient from its time-elongation profile, namely, FPF (Sheeley et al. 2008; Rouillard et al. 2008) and HMF (Lugaz 2010). For a detailed discussion of the FPF and HMF techniques and their application, the reader is directed to Möstl et al. (2011), whose nomenclature is adopted here, but the basic underlying principles of these techniques are noted below.

From purely geometrical considerations, a solar transient propagating anti-sunward in a fixed direction at a constant radial speed will exhibit a unique time-elongation profile dictated by that speed and direction (Sheeley et al. 1999). In consequence, the time-elongation profile of a solar transient as viewed from a single vantage point can be fitted to retrieve these parameters. For mathematical convenience, such analysis is often done based on the premise that the transient geometry in the plane defined by the P.A. of interest (usually the ecliptic plane) is (1) a propagating point source (the Fixed Phi, FP, model, e.g., Sheeley et al. 2008; Rouillard et al. 2008) or (2) an expanding circle anchored at Sun-center by a point on its circumference (the Harmonic Mean, HM, model, e.g., Lugaz 2010). The fitting of time-elongation profiles based on an FP model geometry (i.e.,

Table 1
FPF and HMF Results for CME L

Technique	Speed (km s^{-1})	Longitude (°)	Onset Time (UT on Aug 1)	1 AU Arrival Time (UT)
FPF	698 (673–718)	E3 (E0–E4)	03:42 (03:08–04:03)	12:57, Aug 3 (11:39–14:28, Aug 3)
HMF	858 (814–909)	E36 (E32–E40)	04:55 (04:29–05:20)	03:30, Aug 3 (01:15–05:32, Aug 3)

Note. For each entry we list the average value and, in brackets, the range of values.

FPF) is clearly more applicable to features that are narrow in terms of their extent in the plane of interest and has been applied successfully to longitudinally restricted CMEs and, most notably, small-scale plasma blobs that have become entrained at the stream interface (e.g., Rouillard et al. 2008, 2009). Conversely, fitting time-elongation profiles assuming an HM geometry (i.e., HMF) is more likely to, and indeed has been shown to, produce accurate results for wide CMEs (e.g., Möstl et al. 2011). It should be made clear that both FPF and HMF approaches to fitting single spacecraft time-elongation profiles are bound by the constraints that the radial speed and propagation direction are assumed to be constant over the elongation range used to perform the fit, notwithstanding the inherent simplicity of the assumed model geometries themselves. However, the FPF and HMF techniques have been shown to be successful when applied appropriately, which is particularly heartening given their ease of implementation compared to some of the more complex methods currently in use (as discussed by Möstl et al. 2011). It should also be pointed out that the triangulation of Liu et al. (2010a, 2010b) implicitly assumes an FP model geometry; triangulation based on an HM-like transient geometry has also been investigated (Lugaz et al. 2010), although it is not performed here.

As alluded to in the previous section, for the FPF and HMF techniques to provide accurate results, a time-elongation profile must be of sufficient elongation extent (more than 30° is an often-quoted value; see Möstl et al. 2011). While this was not so for CME M, it is the case for the track of CME L derived from the *STEREO-A*/HI observations. Results from applying HMF and FPF techniques to the five time-elongation profiles for CME L, defined by the points overplotted in Figure 6, are presented in Table 1. For each resultant parameter, namely, radial speed, ecliptic longitude, onset time, and 1 AU arrival time, we list the average value and, in brackets, the range of values. The fitting procedure returns best-fit values for longitude, speed, and onset time, whereas calculation of 1 AU arrival time is simply based on the latter two. The consistency between the results of each of the five separate fits gives us confidence in our ability to track the same feature consistently.

The radial speeds of 698 and 858 km s^{-1} derived for CME L from the FPF and HMF techniques, respectively, indicate that this is a relatively fast CME while highlighting the significant difference in the results obtained from imposing what are intrinsically two extreme model geometries. Moreover, in this case, the two methods yield considerably different propagation directions; a typical CME propagating along a longitude of E3° (obtained from FPF) would likely impact Earth, whereas a CME propagating at E36° (from HMF) would be unlikely to do so. While the onset times are only about an hour apart, the 1 AU arrival times differ by approximately 10 hr. The high-speed outputs by both methods may cast doubt on the validity of the assumption of constant speed inherent in both of these techniques. In fact, applying the FPF and HMF techniques to the time-elongation profile of a transient that has undergone

acceleration/deceleration along any part of its track will lead to erroneous estimates of both its radial speed and propagation direction.

Despite this, as a check of the results presented in Table 1, we note that a comparable analysis performed by C. Möstl et al. (2011, private communication) produced speeds of 672 and 844 km s^{-1} and directions of W3° and E31° for FPF and HMF techniques, respectively. Their results are not significantly different from those listed in Table 1. Their analysis was, however, restricted to elongations greater than 11° (as noted earlier, we exclude elongations below 7°.5). If we redo our fitting, but based on the same minimum elongation of 11°, we obtain speeds and directions of 643 (775) km s^{-1} and W3° (E29°) for FPF (HMF) techniques. Moreover, setting a minimum elongation of 15° yields values of 583 (714) km s^{-1} and W7° (E24°), for FPF (HMF). Progressively increasing the minimum elongation used in our FPF and HMF analysis leads to a corresponding reduction in the best-fit radial speed, which supports the view that the CME is experiencing significant deceleration (possibly due to drag; see Temmer et al. 2012) early on in its passage through the HI field of view. Increasing the minimum elongation also results in the best-fit propagation longitude, from both FPF and HMF techniques, moving progressively eastward (with respect to the Sun–Earth line); this is actually also an artifact of fitting a decelerating velocity profile assuming a constant speed and direction. These results are suggestive of deceleration out to at least 15°. Although potentially we could progressively increase the minimum elongation used in the FPF and HMF in a bid to ascertain the regime over which CME L is decelerating, this, as noted previously, has implications in terms of the accuracy of the fit. Instead, we embark on an adaptation to the FPF and HMF techniques that we believe has not been applied to CME analysis before, in which we relax the constant speed assumption inherent in those methods, while still assuming radial propagation, and deduce what we consider the most appropriate propagation direction based on physical considerations. However, it is first worth noting that the triangulation results for CME L (shown in Figure 5), assuming an FP-like transient geometry, indicate an average radial speed of over 1100 km s^{-1} in the COR2 field of view, consistent with our deceleration hypothesis.

As the assumption of constant radial speed is considered inappropriate for CME L, at least during the early stages of its evolution, we compute radial speed profiles based, instead, on a set of pre-defined propagation directions. Results of this analysis are presented in the panels on the left-hand side of Figure 7. The left-hand panels of Figure 7 present time series of radial speed for a set of 11 fixed propagation directions ranging from E50° to W50°, in steps of 10° (these directions equate to longitude with respect to Earth). The manually selected time-elongation points, overplotted on CME L's track in Figure 6 and used for the FPF and HMF analyses discussed above, are also used to calculate these speed profiles. For each (color coded) longitude, six time series are plotted, one for each of the five sets
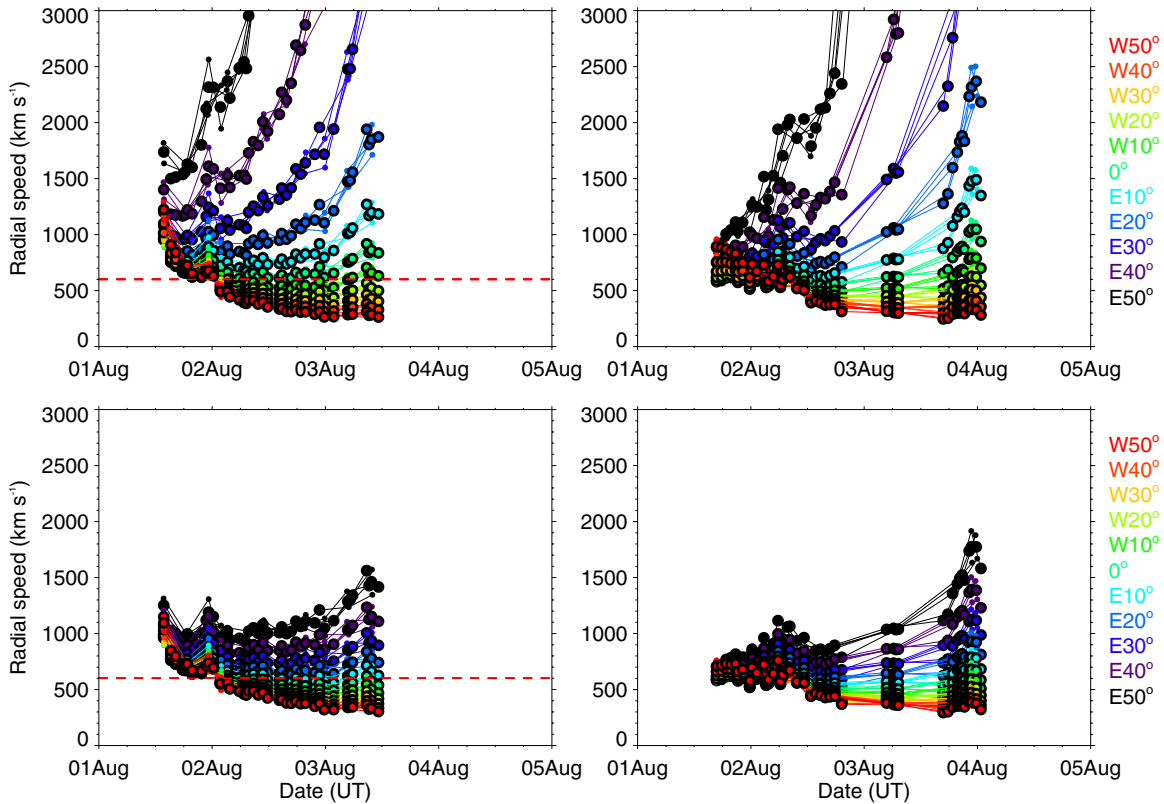
Figure 7. Radial speed profiles derived for CME L (left-hand panels) and CME A (right-hand panels), for a set of 11 fixed longitudes ranging from E50° to W50°, in steps of 10°, for both the FP (top panel) and HM (bottom panel) geometric models. For each (color-coded) longitude, six time series are plotted, one for each of the five sets of manually selected points (marked with small dots), and the other indicating the average radial speed profile (large dots). For CME L (left-hand panels), a red dashed line indicates a speed of 600 km s^{-1}, that being the solar wind speed measured by the near-Earth *Wind* spacecraft after the arrival of the principal shock associated with CME L.

of manually selected points (marked with small dots in Figure 7), and the other indicating the average radial speed profile (large dots). The upper-left panel of Figure 7 assumes an FP model geometry in the calculations; the lower-left panel assumes an HM-type geometry.

These curves provide a remarkable amount of insight into the nature of the CME in question. Perhaps most striking is the fact that many solutions can be rejected on the grounds that they appear unphysical, with prolonged acceleration up to excessive speeds. Of course, it should be borne in mind that this analysis is based on the implicit assumption that the CME propagation is radial over the region of interest. However, we note that the results from geometric triangulation presented in Figure 5, and for an admittedly small number of other CMEs by Liu et al. (2010a, 2010b), present evidence for near-Sun deflection of CMEs. We also note that other studies, in which CME directions are compared to their inferred source region locations, strongly support the view that CMEs can be deflected (e.g., Cremades & Bothmer 2004). The value of the triangulation method is that no assumption is made about the source region. The speed profiles derived for CME L based on the assumption of an FP geometry (upper-left panel) exhibit a seemingly unphysical acceleration over much of the CME's trajectory for all longitudes east of the Sun–Earth line. A similar consideration of the results based on an HM geometry (lower-left panel) would exclude as unphysical propagation along longitudes east of E20°.

As will be shown later in this paper and is discussed more comprehensively by C. Möstl et al. (2012, in preparation), the solar wind speed diagnosed in situ near Earth was around

400 km s^{-1} prior to the arrival (on August 3) of the principal shock associated with CME L. Shock arrival corresponded to an increase in wind speed to 600 km s^{-1} (this value is marked on the left-hand panels of Figure 7 as a red dashed line). Thus, it seems sensible to be guided by that value in terms of identifying a valid solution. This would preclude, as unrealistic, longitudes westward of W20°, which result in final wind speeds of the order of only a couple of hundred km s^{-1}. Thus, an examination of Figure 7 would lead us to the conclusion, based on grounds of physical realism and consistency with other known information, that the propagation longitude of CME L lies somewhere between W10° and W30° for an FP geometry and between E10° and W10° for an HM geometry. That a CME's speed and arrival time, derived from imaging observations, should be consistent with in situ data is an argument central to the work of Rollett et al. (2012)—based on similar ideas propounded by Möstl et al. (2010). Rollett et al. (2012) determined the direction of a CME based on the projected 1 AU arrival time only and found that this resulted in a speed that matched what was observed in situ.

The longitude of propagation deduced for CME L from this analysis is not significantly different for the two model geometries and is generally somewhat westward of what FPF and HMF analysis would suggest (at least based on use of the full time-elongation profile). Note that triangulation (Figure 5) suggests a longitude of propagation for CME L (E15°; albeit calculated in the outer portion of the COR2 field of view) that is near the eastward limit of the range of directions suggested by our "fixed direction/variable speed" analysis illustrated in

Table 2
FPF and HMF Results for CME A, in the Same Format as Table 1

Technique	Speed (km s^{-1})	Longitude (°)	Onset Time (UT on Aug 1)	1 AU Arrival Time (UT)
FPF (full track)	589 (581–600)	W4 (W3–W5)	10:04 (09:54–10:18)	05:50, Aug 4 (04:47–06:41, Aug 4)
HMF (full track)	642 (624–657)	E19 (E16–E21)	10:45 (10:33–11:01)	00:59, Aug 4 (23:48, Aug 4–02:34, Aug 4)
FPF (<30°)	635 (615–683)	E6 (E2–E14)	10:50 (10:35–11:20)	01:48, Aug 4 (21:47, Aug 3–03:32, Aug 4)
HMF (<30°)	680 (645–764)	E25 (E17–E40)	11:05 (10:50–11:31)	22:00, Aug 3 (15:47, Aug 3–00:44, Aug 4)

Notes. For each model geometry, two sets of results are quoted, the first set produced from the full track (4° to 50° elongation) and the second set limited to elongations of less than 30°. For each entry we list the average value and, in brackets, the range of values.

the left-hand panels of Figure 7. The mean width of a CME in P.A. is of the order of 45° (e.g., Gopalswamy 2004a), so, assuming cylindrical symmetry and ignoring projection effects, the latter analysis would imply that the event would almost certainly impinge on Earth, which is, of course, consistent with what is evidenced by various Earth-bound observatories. Our argument that assuming a constant speed is inappropriate for CME L, given its high initial speed and clear evidence for deceleration, means that we feel that the results of the FPF and HMF analyses given in Table 1 should be superseded by the results deduced from Figure 7.

The results shown in Figure 7 (left-hand panels) suggest a radial speed for CME L of the order 1000 km s^{-1} when it first enters the HI-1A field of view. Note that this initial speed is actually not too dissimilar over the entire range of longitudes considered and is consistent with the results of the triangulation. Such a fast CME must have undergone extreme early acceleration, presumably in this case prior to entering even the COR2 field of view. The speed profiles identified as being the most realistic indicate a 12 hr period of fairly rapid deceleration as the CME propagates through the HI-1A field of view, where the CME speed reduces from about 1000 to 800 km s^{-1}, after which only modest deceleration is inferred. The deceleration of CMEs has been the subject of much work since the seminal paper by Cargill (2004). His derivation of the drag force per unit mass requires parameters that can be provided by the above analyses, such as the speed of both the CME and the solar wind, but also requires information on the mass and cross section of the CME. Although the deceleration of CME L by drag could be calculated, there would undoubtedly be an additional complication due to any interaction between CMEs L and M. This is addressed by Temmer et al. (2012).

By around 15:30 UT on August 1, CME L has obscured CME M from the viewpoint of *STEREO-A*, at least at ecliptic latitudes. If we consider the (probable) interaction between the two CMEs as an interaction between two radially extended magnetic systems, i.e., an interaction between two likely magnetic flux ropes of which the bright leading loops form only a part, then we have a highly complex situation to consider. What we can say is that the period of extreme deceleration in L is consistent in time with the interval over which that interaction may be assumed to occur. We can also say that the above analyses suggest that M is propagating at a longitude around E20°, and that L is likely directed some 30° west of M. For a typical CME extent (Gopalswamy 2004a; Bothmer & Schwenn 1998), this would mean that although the CMEs might not be wholly aligned in terms of their longitudinal and latitudinal extents, there would be a substantial overlap and, thus, a significant interaction. Such an interaction could quite conceivably alter the direction of motion of any surviving CME structure.

We believe that the assessment of CME kinematics based on the calculation of radial speed profiles over a range of fixed propagation directions, as illustrated in Figure 7, is the first demonstration of this kind of analysis, and that it can be a powerful tool in the investigation of solar transient propagation characteristics.

2.2.3. CME A

The ecliptic signature of CME A, which enters the HI field of view after L and propagates mainly north of the ecliptic plane, is indicated in Figures 3 and 6 with a yellow dashed line. Overplotted on CME A's track in Figure 6 are five sets of manually selected points tracing the CME front. The track extends out beyond the elongation of Earth but does become indistinct between 30° and 40° elongation where no attempt has been made to trace it. In the same way as was done for CME L, we have used the FPF and HMF analysis techniques to provide estimates of radial speed, ecliptic longitude, onset time, and 1 AU arrival time for CME A. In addition to fitting the full ecliptic time-elongation track for A, we have also separately fitted that part of the track at elongations below some 30°, i.e., below our self-imposed data gap, in an attempt to verify whether the track segment crossing Earth's elongation is indeed a continuation of A. The results are given in Table 2. Noting the arguments given previously concerning the accuracy of the FPF and HMF procedures, this cannot be viably done by attempting to fit just the small section of track above 40°.

FPF (HMF) analysis of the full and restricted time-elongation profiles produces speeds that are within some 46 (38) km s^{-1} and longitudes within 10° (6°) of one another. From this we tentatively conclude that the section of track crossing the elongation of Earth is, indeed, a continuation of the signature of CME A. The FPF analysis of the full track suggests that, in terms of its longitude of propagation, CME A is closely Earth directed, heading just 4° west of the Earth. HMF analysis gives a propagation direction 19° east of Earth. Given our knowledge of the approximate longitude of propagation of CME A, we can deduce from the HI-1A images that the apex of CME A is actually directed some 10° north of the ecliptic plane. FPF and HMF analyses of the full ecliptic track yield radial speeds for CME A of 589 and 642 km s^{-1}, respectively, as well as projected onset times within 45 minutes and 1 AU arrival times within 5 hr of each other. While this analysis implies that CME A is propagating significantly slower than CME L, its relatively high speed does suggest that it is worthwhile performing the same "fixed direction/variable speed" analysis as was done in the previous section for CME L; this we do using the full time-elongation track. We show these results in the right-hand panels of Figure 7.
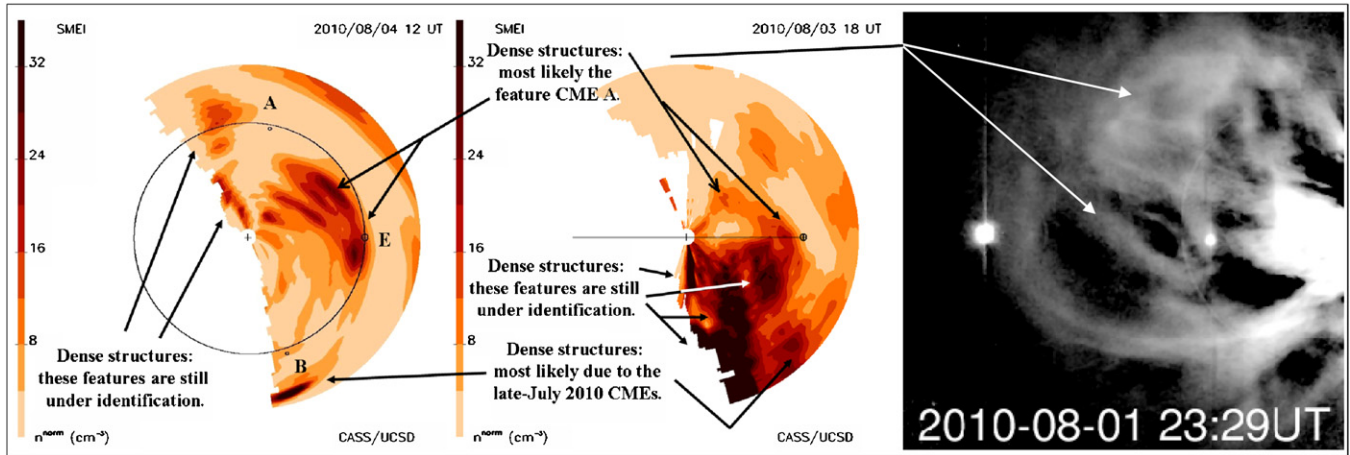
Figure 8. Preliminary results of the UCSD three-dimensional density tomography reconstruction based on the use of SMEI data as input. The left-hand panel displays an ecliptic cut through the three-dimensional density reconstruction, at 12:00 UT on August 4, with the Sun (+) at the center, the Earth (E) on the right, along with its orbital path, and both *STEREO* spacecraft (labelled *A* and *B*). The central panel presents a meridional cut of density, at 18:00 UT on August 3 (in the plane defined by Earth's central meridian). The Sun is, again, at the center, the Earth on the right, and the projection of Earth's orbital path lies across the center of the image. The right-hand panel presents a background-subtracted HI-1A image from 23:29 UT on August 1.

The same argument as was used previously regarding unphysical acceleration leads us to again reject the possibility that CME A is propagating east of the Sun–Earth line particularly in the case where an FP geometry is assumed (Figure 7, upper-right panel), but also for an HM geometry (Figure 7, lower-right panel). FP solutions for longitudes around W10° suggest either only a modest deceleration or a near-constant speed consistent in value with the FPF results given in Table 2. Similarly, for the HM case, near-Earth-directed longitudes appear to produce the most physically realistic speed profile, with values in line with that from the HMF analysis. This supports the idea that FPF and HMF analyses are more appropriate in this case than for CME L, at least in terms of their requirement for a constant speed. We should point out, however, that inspection of the speed profiles from the HM version of this analysis (depicted in the lower-right panel of Figure 7) leads us to suggest a more westerly propagation direction for CME A than the results from HMF analysis (presented in Table 2) would imply.

It is worth noting that FPF analysis performed by C. Möstl et al. (2011, private communication) for CME A produces results for radial speed and longitude (598 km s^{-1} and W11°, respectively) that are highly consistent with the analogous values in Table 2. However, their HMF results, 601 km s^{-1} and W12°, differ from those quoted in Table 2 (derived from the full time-elongation profile) by 41 km s^{-1} and 31°. Their value for the HMF longitude is, in fact, more consistent with what is inferred based on the results shown in Figure 7 (lower-right panel).

2.2.4. CME B

The ecliptic track of CME B, the last major CME in the series, appears to extend out to the elongation of Earth (see Figures 3 and 6, dashed orange line), although becoming somewhat less distinct at elongations beyond 40°. For this reason, we apply the FPF and MHF analysis techniques to the full time-elongation track and, separately, only to elongations below 40°. Overplotted on CME B's track in Figure 6 are the five sets of manually selected points tracing its front.

FPF analyses of the full and truncated time-elongation profiles for B produce radial speeds and longitudes (as presented in Table 3) that are within 27 km s^{-1} and 13° of one another,

which may suggest that what we are tracking beyond 40° is indeed the continued track of CME B. HMF analysis yields slightly more significant differences: 67 km s^{-1} and 36° (again see Table 3). Comparable analysis performed by C. Möstl et al. (2011, private communication) yields speeds and longitudes of 574 km s^{-1} and W8° for FPF and 594 km s^{-1} and E6° for HMF analysis. For both geometries, speed and longitude results are within 18 km s^{-1} and 6°, respectively, of what we derive (based from the full track and quoted in Table 3). These (and previously quoted results for CMEs L and A) reveal, at least, a basic consistency between the identification of tracks and the slightly different approaches to the curve fitting used within the two institutes.

Like in the case of CME A, the results of FPF and HMF analyses suggest a speed for CME B that exceeds the typical slow solar wind speed (300–350 km s^{-1}), so the same "fixed direction/variable speed" approach that was applied to CMEs L and A is also applied here. Conclusions drawn on the basis of results of such analysis (not shown), performed using the full time-elongation track, are perhaps unsurprisingly identical to those for CME A (i.e., it appears that applying FPF and HMF analyses to this event is valid).

2.3. SMEI Observations: Preliminary Results

The analysis of the visible-light heliospheric images from the SMEI instrument on the *Coriolis* spacecraft, results of which are presented here, employs the University of California, San Diego (UCSD), three-dimensional (3D) computer-assisted tomography analysis chain as used by, for example, Bisi et al. (2008) and Jackson et al. (2010a) and detailed by Jackson et al. (2010b, 2011), and references therein. Thus far, only a preliminary analysis has been performed, independent of the *STEREO*/HI analyses discussed above. A tomographic reconstruction of the inner heliosphere—with a 3°.3 resolution in latitude and longitude, a 6 hr temporal resolution, and taking, as input, the UCSD-processed SMEI data—resolves multiple structures in the reconstructed plasma density.

An ecliptic cut through the resultant 3D density reconstruction, corresponding to a time of 12:00 UT on 2010 August 4, is displayed in the left-hand panel of Figure 8. The central

Table 3
FPF and HMF Results for CME B, in the Same Format as Table 1

Technique	Speed (km s^{-1})	Longitude (°)	Onset Time (UT on Aug 1)	1 AU Arrival Time (UT)
FPF (full track)	562 (553–568)	W9 (W8–W11)	16:45 (16:24–16:59)	15:49, Aug 4 (15:18–16:36, Aug 4)
HMF (full track)	612 (598–626)	E12 (E9–E14)	17:49 (17:31–18:07)	11:06, Aug 4 (09:54–12:18, Aug 4)
FPF ($<40°$)	535 (532–543)	W22 (W17–W25)	15:10 (14:51–15:51)	17:48, Aug 4 (17:24–18:01, Aug 4)
HMF ($<40°$)	545 (541–554)	W24 (W12–W27)	15:53 (15:35–16:37)	17:08, Aug 4 (16:41–17:23, Aug 4)

Notes. For each model geometry, two sets of results are quoted, the first set produced from the full track (4° to 52° elongation) and the second set limited to elongations of less than 40°. For each entry we list the average value and, in brackets, the range of values.

panel of Figure 8 presents a meridional cut, for 18:00 UT on August 3. For comparison, a background-subtracted *STEREO*/HI-1A image from an earlier time, 23:29 UT on August 1, is presented in the right-hand panel. Relevant features are marked on the appropriate panel and noted in the figure caption. Densities reconstructed using the SMEI data are compared to the visible-light signatures, in particular for CME A, observed by *STEREO*/HI.

The dense, Earthward-bound plasma structures that are reconstructed in that region of the ecliptic plane bounded by the Sun–Earth and Sun–*STEREO-A* lines (Figure 8, left-hand panel) are likely to be associated with CME A, observed earlier by *STEREO-A*/HI (right-hand panel). Consistent with the HI observations (right-hand panel), the tomographic results suggest a propagation direction for A slightly north of the ecliptic plane (central panel). Other structures in the same longitude sector, but propagating behind the main identified front, may be associated with the sub-structure within CME A that is also evident in the HI images; this requires further investigation. The 1 AU arrival time of the main front based on the tomographic reconstruction is, in fact, consistent with what is predicted for CME A from the *STEREO*/HI analyses presented in Section 2.2.3. Moreover, the reconstructed near-Earth arrival time compares well with the arrival time gleaned from in situ measurements, although the magnitude of reconstructed density is higher than is measured in situ; this again warrants further investigation.

The high-density material to the south of the ecliptic plane (central panel) and the feature to the east of the *STEREO-B* spacecraft (left-hand panel) were originally disregarded due to thoughts that they were an artifact of the analysis technique. Closer examination of the *STEREO*/HI images taken prior to August 1 suggests that they may be associated, instead, with CME activity that occurred during late July. These late July CMEs, along with a comprehensive analysis of the SMEI observations and a global, heliospheric perspective of the four August CMEs, are presented in Webb et al. (2012).

2.4. Coronagraph and EUV Imaging Observations

Our analysis thus far has mainly been driven by the *STEREO*/HI observations, from which we have identified and defined the basic characteristics of each of the sequence of CMEs, as well as endeavouring to ascertain their kinematic properties. We have also performed a preliminary comparison of the *STEREO*/HI observations, taken from a vantage point well away from the Sun–Earth line, with heliospheric imaging performed from Earth orbit by SMEI. We now extend our analysis through the introduction of further data sets.

In this section, we present a brief examination of images taken by the *STEREO*/EUVI, COR1, and COR2 instruments

(Howard et al. 2008), in a bid to associate what is observed in the inner heliosphere by HI with chromospheric/coronal activity diagnosed by the other SECCHI imagers, not least to explore the CME onset process. To this end, Figure 9 presents a (non-consecutive) sequence of images taken by the EUVI instrument on *STEREO-A* in 304 Å (corresponding to the He II line), characteristic of the solar chromosphere. Figures 10 and 11 show a selection of background-subtracted images from the *STEREO-A*/COR2 and *STEREO-A*/COR1 instruments, respectively. Note that the ecliptic plane projects to the horizontal center line in all of these images.

The EUVI image taken at 02:36 UT on August 1 (Figure 9, top-left panel) reveals the two principal features of the Earth-facing northern hemisphere chromosphere, although as viewed from the vantage point of *STEREO-A* located 78°.3 west of the Sun–Earth line. These features, two large prominences (labeled FI_1 and FI_3 on this panel to be consistent with the notation adopted by Schrijver & Title 2011), occupy large channels extending beyond the limb. The subsequent image, from 03:06 UT (top-right panel), shows a prominence eruption on the limb south of FI_3 (we label this prominence FI_0 although this notation was not used by Schrijver & Title 2011). By 03:36 UT (middle-left panel), the FI_0 prominence material has propagated out to the edge of the EUVI field of view. Note that an EUVI image taken at 02:56 UT (not shown) clearly shows the initial stages of this eruption. The time of the eruption of FI_0 and its location over the east limb as viewed from *STEREO-A* are consistent with it being associated with CME M (the back-projected onset time of which was estimated from triangulation to be around 02:42 UT; see Section 2.2.1).

This event is manifest in the *STEREO-A*/COR2 image taken at 04:09 UT as a small CME (Figure 10, top-left panel), which first entered the field of view some 30 minutes earlier. The location and angular extent of this CME as seen by COR2, as well as its basic morphology, are consistent with the HI-1A observations of CME M. Estimates of the longitude of propagation and radial speed of this CME based on polarimetric localization of the COR2 observations (de Koning and Pizzo 2011), E19° ± 8° and 616 ± 26 km s^{-1}, respectively, are in reasonable agreement with the results of the triangulation analysis presented in Section 2.2.1.

The next incidence of significant activity that was observed by EUVI on *STEREO-A* was the eruption of prominence FI_1, which is illustrated in the bottom-left panel of Figure 9 (09:16 UT on August 1). While its precise timing is not clear due to an extended period of prior uplifting, the eruption appears to be underway by 08:16 UT.

For further clarification regarding this later interval, we also look to the coronagraph data. A CME, exhibiting a well-defined loop-like structure, is clearly observed by *STEREO-A*/COR1 at
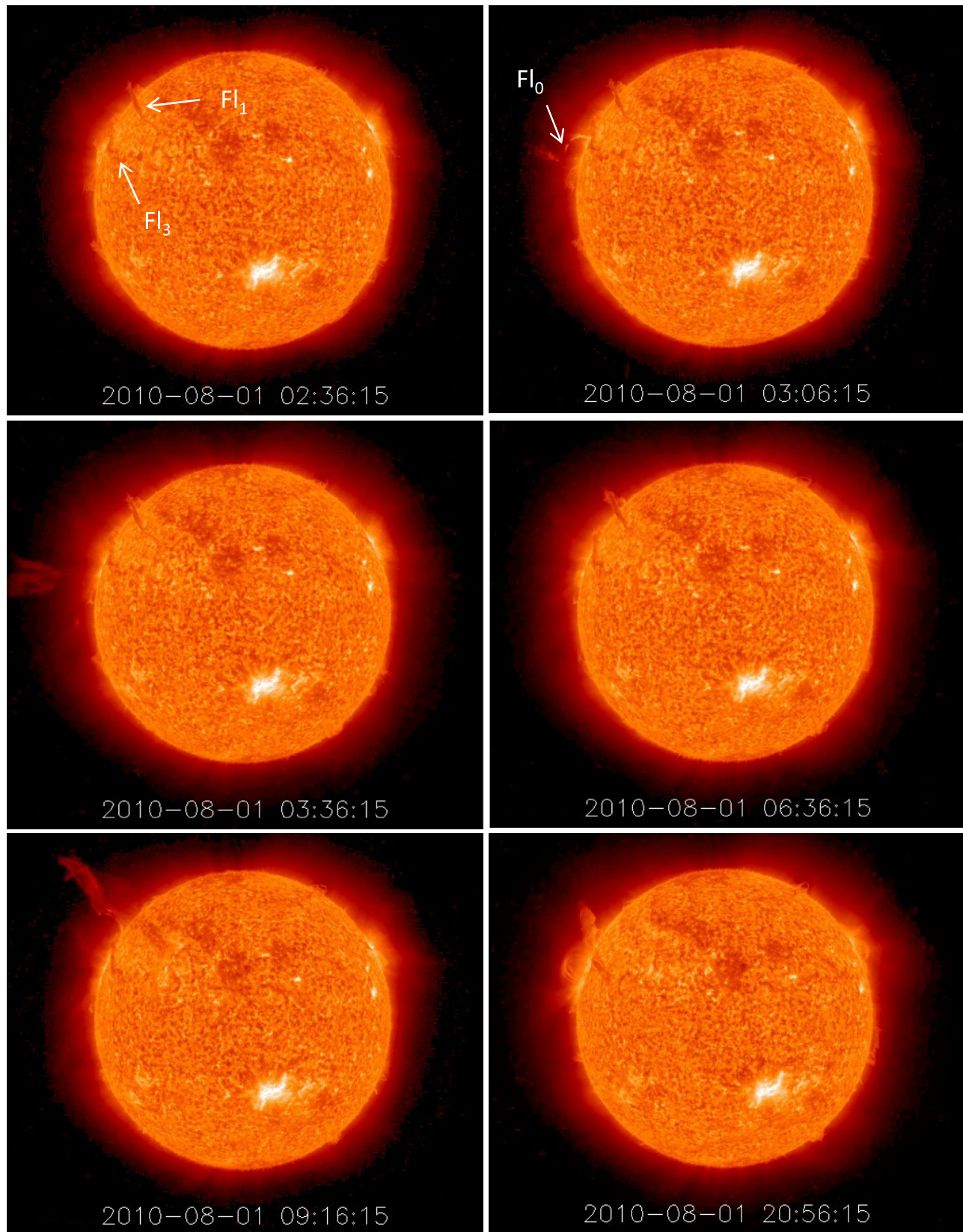
Figure 9. Selection of six EUV images, taken by the EUVI instrument on the *STEREO-A* spacecraft in the He II $\lambda 304$ emission line on 2010 August 1, in each case with the time of the exposure indicated. The locations of the two major filaments, FI_1 and FI_2, are marked, as is a filament on the east limb (FI_0). The ecliptic plane corresponds, approximately, to a horizontal line across the center of each image.
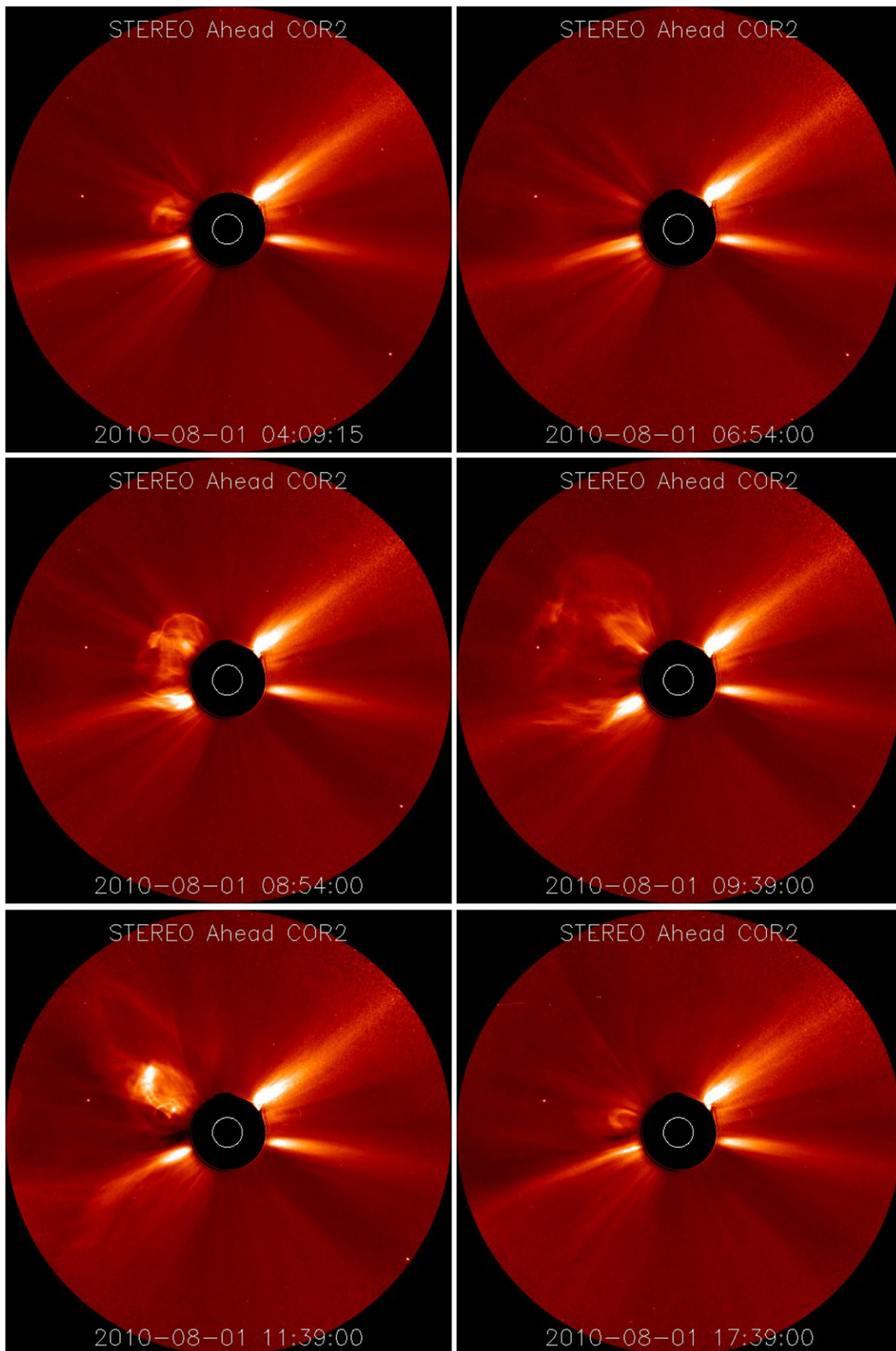
Figure 10. Selection of six *STEREO-A*/COR2 coronagraph images from 2010 August 1. The ecliptic plane corresponds to the horizontal center line of the images.
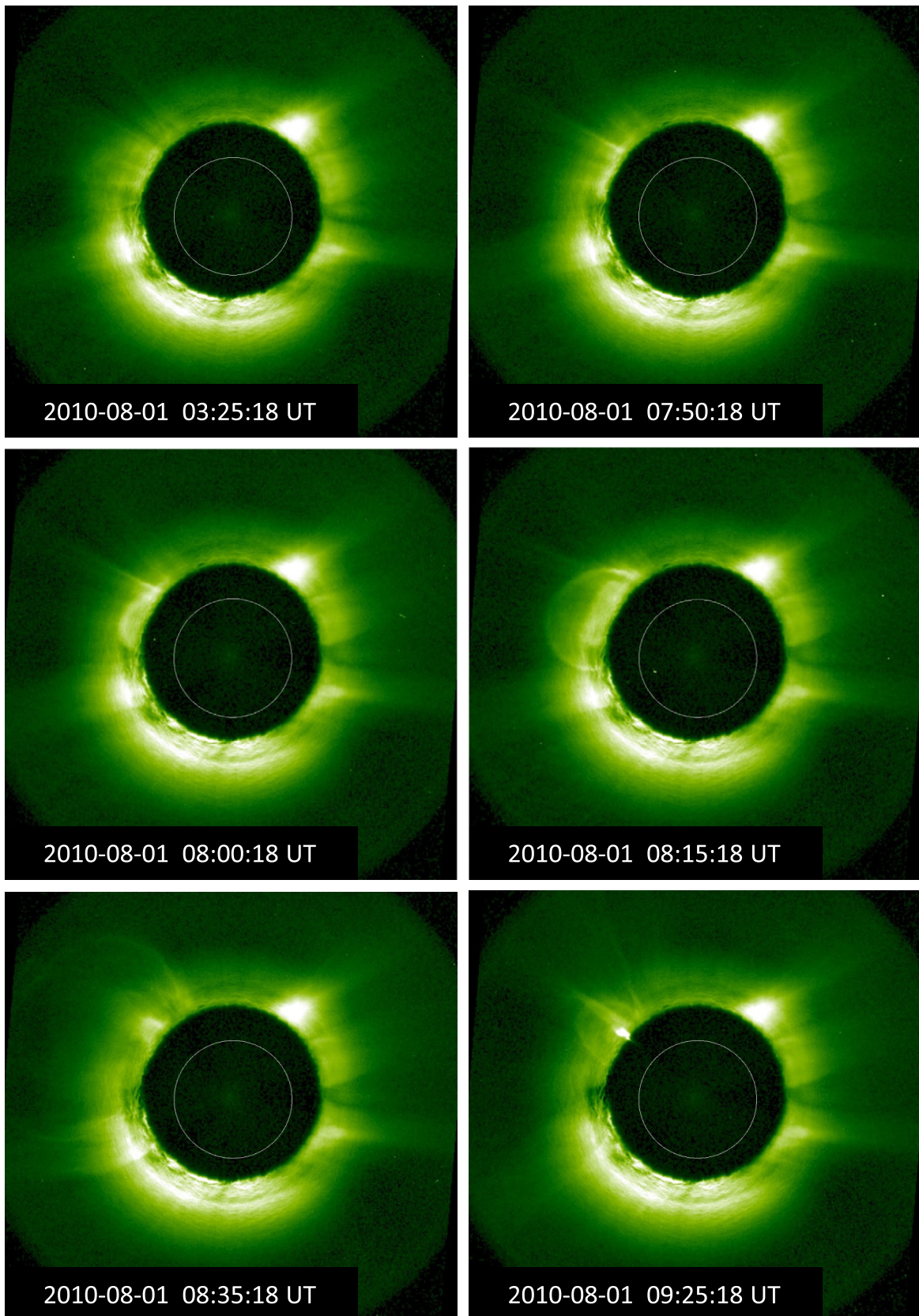
Figure 11. Selection of six *STEREO-A*/COR1 coronagraph images from 2010 August 1. The ecliptic plane corresponds to the horizontal center line of the images.

08:15 UT (Figure 11, middle-right panel), having entered the COR1 field of view at around 07:50 UT (top-right panel). By 08:54 UT, this CME has propagated well into the COR2 field of view (Figure 10, middle-left panel). The center of the CME propagates in a direction approximately 20° north of the ecliptic in the image plane, although the large P.A. span of the CME makes it quite difficult to ascertain this precisely. At 08:35 UT (Figure 11, bottom left), as the front of this CME is approaching the outer edge of the COR1 viewing area, a second narrow CME can be seen emerging into the field of view at a P.A. just south of its northern edge. This second CME—a narrow loop that appears to be directed 30° north of the ecliptic in the image plane—is clearly viewed later in its propagation by COR2 (for example, in the bottom-left panel of Figure 10 at 11:39 UT). It is this second, narrow CME that we suggest contains the material associated with the eruption of prominence FI$_1$.

So, summarizing the latter interval, COR1 and COR2 image two loop-like CMEs propagating north of the ecliptic plane. The first CME enters the COR1 field of view around 07:50 UT; the second much narrower CME, which enters the COR1 field of view at 08:35 UT, appears to be carrying the erupting prominence material of FI$_1$ observed by EUVI.

We note that the onset times, derived from FPF (HMF) analysis of HI time-elongation profiles, were 03:42 (04:55) UT for CME L (see Table 1) and 10:04 (10:45) UT for CME A (see Table 2); all of these times are on August 1, and in the case of CME A the values are those derived from the full J-map track. Of course, these onset times are very approximate as their calculation neglects the possibility of any near-Sun acceleration or deceleration. Any discrepancy resulting therefrom is likely to be worse for CME L, which appears to decelerate rapidly even as it enters the HI field of view. The later back-projected onset time derived for CME L by triangulation (07:48 UT) is arguably more accurate than what is quoted above since it is based on observations made closer to the Sun. In fact, this onset time estimate for CME L is close to the time that the first of the two aforementioned CMEs enters the COR1 field of view (07:50 UT); thus, we identify that CME as L. There may be some evidence that between the COR2 and HI-1 fields of view, CME L has undergone a deflection in latitude toward the ecliptic. Meanwhile, the second, narrow northward-propagating CME, with embedded prominence material, can only be CME A.

On August 1, *GOES* detected a C3.2 flare in integrated 1–8 Å X-ray flux, with onset, peak, and end times listed as 07:55 UT, 08:26 UT, and 09:35 UT, respectively. These timings were confirmed by ground-based observations in Hydrogen alpha (H alpha), which also provided a location for the flare in AR 11092. The times of the onset and peak of the flare, deduced from both the X-ray and H-alpha observations, correspond closely with the time at which prominence FI$_1$ erupts. Both the location and timing of the flare suggest that it is very closely associated with the CME that emerges into the COR1 field of view at 07:50 UT (identified above as CME L), although the CME is clearly already visible at flare onset and has reached an elongation of some 1°.5 by the time that the flare peaks. The detailed relationship between the flare and CME L, including an analysis of associated coronal dimming, is presented by Temmer et al. (2012).

Polarimetric localization, again based on the COR2 data, suggests that the CME L propagates in a direction defined by a longitude of E41° ± 5° and a latitude of N22° (i.e., 22° north of the ecliptic plane). The radial speed deduced on the basis of this direction of travel is 1274 km s^{-1}, which is in reasonable agreement with the (albeit ecliptic) value yielded by triangulation of COR2 data (see Figure 5) and the speed derived early on its propagation through the HI field of view (again in the ecliptic plane) by our novel fixed direction/variable speed approach (see Figure 7). The northward-oriented trajectory of CME L, derived from the polarimetric localization analysis of COR2 data, is consistent with what is deduced from examination of the COR2 images themselves. We reiterate our previous suggestion that the CME subsequently undergoes a deflection toward the ecliptic plane. The longitude derived by polarimetric localization, however, appears significantly more eastward than the bulk of the analysis presented in Section 2.2.2 leads us to believe.

Applying the polarimetric localization analysis to the COR2 feature that we identify as being CME A, which carries the erupting prominence material of FI$_1$, suggests propagation in a direction N22°/W21° ± 3° at a radial speed of 644 ± 49 km s^{-1}. This speed is not inconsistent with the results of the HI-based techniques (Section 2.2.3), despite the fact that the latter make use of ecliptic observations, but the longitude is rather more westward than analysis of HI data might suggest.

The eruption of prominence Fl$_3$ is clearly already well underway at 20:56 UT (Figure 9, bottom-right panel). Over the previous hours, the prominence had undergone significant lifting and activation. Again, it is hard to define an exact time for the eruption, but the prominence could be clearly seen to ascend rapidly somewhat prior to 18:00 UT. This timing may suggest a link between the eruption of prominence FI$_3$ and the launch of CME B (estimates of onset timings for the latter, derived from HI observations, are given in Table 3). Given the location of FI$_3$ in the EUVI images, 30° north of the ecliptic, one might suggest that any associated CME would emerge from a similar latitude. The final COR2 image presented in Figure 10 (bottom right), from 17:39 UT, reveals a small loop erupting from a location slightly north of the ecliptic, which we identify as CME B. The longitude of propagation of CME B derived from polarimetrc localization of COR2 observations (W6° ± 14°) is consistent with the results presented in Section 2.2.4, although both the latitude and radial speed results produced by the technique (S14° and 805 ± 47 km s^{-1}, respectively) appear rather at odds with previously stated results.

In this section, we have established clear associations between the CMEs identified initially from the HI observations, as well as their manifestations in COR1 and COR2 images, and features that are observed at the Sun in EUV, the latter including three prominence eruptions and a flare.

2.5. STEREO S/WAVES Radio Observations

Each *STEREO* spacecraft carries an identical *STEREO*/WAVES (*S*/WAVES) instrument that measures radio emission and in situ plasma waves (Bougeret et al. 2008) using three orthogonal monopole electric antennae (Bale et al. 2008). *S*/WAVES monitors the frequency range 2.5 kHz to 16.025 MHz, but here we will concentrate on data from the high-frequency receiver (HFR), which covers the range 125 kHz to 16.025 MHz. *S*/WAVES data from *STEREO-A* and *STEREO-B*, acquired between 07:00 and 11:00 UT on 2010 August 1, are shown in panels (a) and (b) of Figure 12, respectively. We note that the gap in the *S*/WAVES data from *STEREO-B* that starts just before 10:30 UT is due to the overall data telemetry loss discussed above. There are several differences between the *S*/WAVES HFR observations made by the two spacecraft.
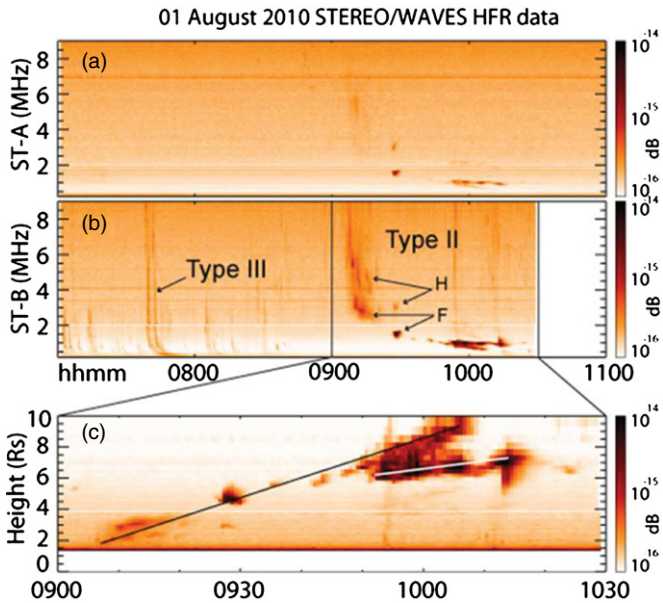
Figure 12. *S*/WAVES HFR observations from 07:00 to 11:00 UT on 2010 August 1 taken from *STEREO-A* (*ST-A*; panel (a)) and *STEREO-B* (*ST-B*; panel (b)) in receiver units and a corresponding time-height plot of a subset of the ST-B data (09:00 to 10:30UT; panel (c)). The black line in panel (c) indicates the emission generated by CME L (slope 1500 km s^{-1}); the white line appears to correspond to the emission created by the interaction between CME L and CME M (slope 600 km s^{-1}).

Between 07:00 and 09:00 UT, *STEREO-B* observed a number of fast-drifting type III radio bursts, whereas *STEREO-A* observed only quiet background. This implies that the source of the type III emission is on the east of the solar disk as viewed from Earth; during this interval, a number of small flares were observed by *SDO*, as described by Schrijver & Title (2011). At 09:08 UT, strong radio emission drifting from high to low frequencies was observed at both spacecraft, but particularly at *STEREO-B*. Both fundamental (F) and harmonic emission (H) was observed (for example, the patch of emission just before 09:30 UT that was detected at 1.5 and 3 MHz, simultaneously). This radio emission corresponds to a type II burst, driven by a fast-moving CME (Gopalswamy 2004b). A similar recent example of a CME-driven metric type II burst is given by Liu et al. (2009).

Panel (c) of Figure 12 illustrates a time–height analysis of the *S*/WAVES HPF data from *STEREO-B* over a more restricted time interval, extending from 09:00 to 10:30 UT on August 1. Frequencies are converted into plasma densities according to the standard relationship $f = 8.98 \times 10^3 (n_e)^{1/2}$, where frequency is quoted in Hz and density in units of cm^{-3}. The density is then converted to distance from the Sun, here using the Alvarez density model (e.g., Leblanc et al. 1998). The lowest radio frequencies presented here correspond to heights of up to some 10 R$_S$. Based on the spacecraft configuration at this time, a height of 10 R$_S$ corresponds to an elongation angle of around 2°–3°. Results of *S*/WAVES analysis are, therefore, directly comparable with results of COR2 and near-Sun HI-1 analyses. Analysis of the time–height plot shows that the radio emission between 09:10 and 10:10 UT rises at a speed of around 1500 km s^{-1} (black line). Consequently, this type II radio emission is evidently associated with CME L.

At 09:50 UT, there is a distinct change in the structure of the type II emission. Emission at the fundamental frequency appears to divide into two branches, with different slopes, implying

the simultaneous existence of radio emission sites moving with different speeds. This has been analyzed in detail by Martinez Oliveros et al. (2012), who concluded that this feature is created by the interaction of two CMEs (Gopalswamy et al. 2001, 2002; Gopalswamy 2004b). In their nomenclature, CME1 and CME2 correspond to the CMEs here labeled as M and L, respectively. In Figure 12c, the second branch of the radio emission observed between 09:50 and 10:15 UT rises at a speed of some 600 km s^{-1} (white line). The onset of this emission appears to correspond to the time at which an interaction between CMEs L and M might be expected to commence (Martinez Oliveros et al. 2012). Martinez Oliveros et al. (2012) also use direction finding to show that the source of the radio emission was located to the east of the Sun–Earth line, consistent with the results presented earlier in the paper.

It is of interest to note that prior to their interaction, only CME L generated significant type II radio emission. This is consistent with statistical observations indicating that only fast CMEs (with speeds greater than 900 km s^{-1}) generate type II emission (Gopalswamy et al. 2003; Gopalswamy 2004b). The estimate of the radial speed of CME M derived by triangulation (732 km s^{-1}; Section 2.2.1) is consistent with the idea that CME M was not traveling sufficiently fast to generate type II emission.

Although the imaging observations suggest that interaction between CMEs L and M would extend over a number of hours, the radio emission associated with this interaction is relatively short-lived. *STEREO-A* does not appear to observe further emission after 10:20 UT, although its location on the west limb may mean that it did not receive any emitted radio emission. The data gap on *STEREO-B* unfortunately precludes further investigation into the duration of the radio emission compared to the extent of the entire interaction.

2.6. SDO Observations

The interval at the start of 2010 August was of particular interest to solar physicists as it represented one of the first periods of significant solar activity since the launch of the NASA *SDO* spacecraft. From its Earth-orbiting platform, *SDO* offers complementary high-resolution imaging. A detailed examination of both flare and eruptive activity on the solar disk on 2010 August 1 is presented by Schrijver & Title (2011), based principally on observations from the *SDO*/AIA (Atmospheric Imaging Assembly) and HMI (Helioseismic and Magnetic Imager) instruments.

Figure 13 shows a solar image taken by the *SDO*/AIA instrument in EUV on August 1 (left-hand panel) that is, of course, on an Earth-orbiting spacecraft viewing activity on the solar disk facing the Earth. Some of the relevant features, as identified by Schrijver & Title (2011), are marked on the image. The image presented here—a narrowband image centered on Iron (Fe) IX/X lines revealing the million degree corona—shows a complex active region system in the northern hemisphere, east of central meridian. In addition, the image clearly shows a pair of highly extended filaments in the northwest, with one following the southern boundary of a coronal hole and the second to the south of the first. Schrijver & Title (2011) denoted these two as FI$_1$ and FI$_3$, respectively. Two major active regions, AR 11092 and AR 11094, contribute to the overall state of the Earth-facing northern hemisphere at this time. Schrijver & Title (2011) developed a model for the prevailing magnetic configuration and its evolution, stressing the large-scale and remote effects of evolving structures.
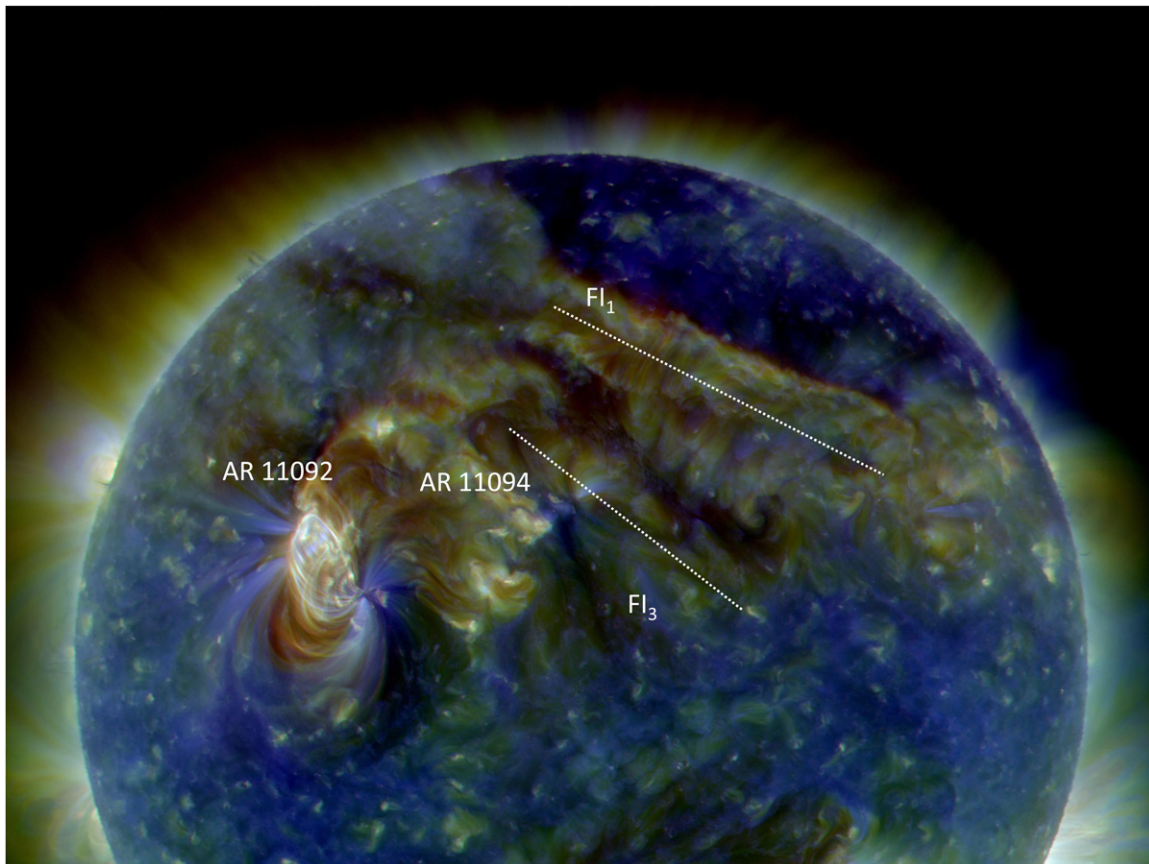
Figure 13. *SDO*/AIA EUV image of the solar disk taken at 12:13 UT on 2010 August 1, with the salient features marked, as identified by Schrijver & Title (2011).

In their Table 1, Schrijver & Title (2011) present a timeline of salient events observed by *GOES*, *SDO*/AIA, *STEREO*/EUVI, and *STEREO*/COR1 on August 1 (and early 2). In Table 4, we summarize the more relevant listings, mainly pertaining to the eruptive and explosive events, although we do include their comments based on *GOES* data. In the final column of our table, we highlight the potential associations between the events listed by Schrijver & Title (2011) and those that we concentrate on in this work.

The *SDO*/AIA entry for 02:40 UT in Table 4 corresponds to the small filament eruption that we discuss in Section 2.4 that was denoted as Fl_0 and was clearly associated with CME M. Schrijver & Title (2011) identify this filament as being associated with AR 11094, located at E10°. A source region at this longitude is consistent with the results of the triangulation analysis, presented in Section 2.2.1 above, which indicate an initial propagation longitude for CME M of E12°.

Based on the AIA observations, Schrijver & Title (2011) list a time for the activation and apparent rise of Fl_1 of 06:30 UT. The lifting of filaments can be gradual, such that specifying an onset time can be rather subjective and uncertain. However, inspection of the COR data, as discussed above, suggests that the eruption itself was underway by 08:16 UT. Table 4 lists 06:40 UT as being the start time of a *GOES* B3 precursor that brightens into a C3 flare at 07:23 UT (and subsequently peaks at 09:00 UT). EUV observations from *STEREO-A* provide a fairly consistent timing estimate for activation of Fl_1, i.e., significant lifting of the filament associated with minor flaring, leading to eruption at about 08:16 UT and a coincident C-class flare.

In Section 2.4, we deduce that this filament eruption is associated with the launch of CME A and also suggest that the flare is associated with CME L. AIA and HMI observations, which given the vantage point of *SDO* provide us a somewhat better opportunity for resolving the on-disk features during this particular interval than *STEREO*/EUVI, might then lead us to infer that CME L would be launched from a site somewhat east of A. However, this assumes, perhaps naively, that a CME would be launched centrally over its associated active region or filament channel; spatial asymmetries in such associations have been recognized for many years (e.g., Harrison 1995, 2009).

Schrijver & Title (2011) state that prominence Fl_3 starts to rise more rapidly at 19:30 UT, again founded on *SDO*/AIA observations. In Section 2.4, from the *STEREO*/EUVI images, we suggest that the prominence can be clearly seen to start ascending rapidly somewhat earlier, around 18:00 UT. The discrepancy between these two estimates could be a function of inherently different viewing geometries. Despite this, we still feel that, given the onset times and longitudes derived for CME B (quoted in Section 2.2.4), this CME is associated with the eruption of Fl_3.

2.7. Arrival at Earth

We now assess the possibility of Earth impact, for each of the four major CMEs in turn. To this end, we make use of in situ measurements made by the near-Earth *Wind* spacecraft (Lepping et al. 1995; Ogilvie et al. 1995), which is currently orbiting the L1 Lagrangian point in the Sun–Earth system. The top six panels

Table 4
Timeline of the GOES Events and the Principal Eruptive/Explosive Events Observed by *SDO* on 2010 August 1 (Adapted from Schrijver & Title [2011])

Time (UT on Aug 1)	*SDO/GOES* Event	Associations/Notes
00:23	*SDO*/AIA: flare-like brightening (feature located at B_2).	. . .
01:40	*GOES*: start of initial rise into B3 flare.	. . .
02:40	*SDO*/AIA: eruption of small filament FI_0 in AR 11094 (location *A*; E10°). AR begins to erupt at 02:17 UT, with nearby dimming from 02:24 UT.	Associated with EUVI He II prominence eruption from 02:56 UT. Appears to be related to CME M.
02:59	*GOES*: start of B2 precursor brightening into short-duration B3 flare.	. . .
06:30	*SDO*/AIA: large northern polar crown filament FI_1 (extending E10° to W40°) shows activation and apparent rise at location B_1. Preceded by lifting and activation at B_1 and elsewhere.	FI_1 activation and eruption observed by *STEREO-A*/EUVI (eruption at 08:16 UT). Associated with CME A.
06:40	*GOES*: start of B3 brightening (precursor to C3 flare noted below) apparently associated with filament activation in AR 11092 (B_2) and with a remote flare in AR 11095 (*H*; east limb).	B3 brightening associated with H-alpha sub-flare at N20°/E36°, and CME L. Note we quote listed onset time of 07:55 UT in Section 2.4.
07:23	*GOES*: start of rise into C3 flare; flare peaks at 09:00 UT.	We quote listed start and peak timings of 08:26 and 09:35 UT, respectively, in Section 2.4.
12:40	*GOES*: start of B5 brightening on flank of C3 flare.	. . .
15:00	*SDO*/AIA: small filament FI_2 rises and erupts (north–south directed filament west of FI_1 at W40°; location *F*).	. . .
16:08	*GOES*: start of B4 brightening; potentially associated with apparently simultaneous AR 11092 (B_3) and/or AR 11095 (*H*) brightening.	. . .
19:30	*SDO*/AIA: filament FI_3 appears to rise more rapidly (filament running east–west, W00° to W20°, south of but parallel to FI_1; location *G*).	FL_3 eruption observed by *STEREO-A*/EUVI near 18:00 UT. Associated with CME B.

Notes. Notation follows that used by Schrijver & Title (2011). Location identifiers for *SDO*/AIA events are given in italics for clarity.

of Figure 14 present magnetic field and bulk proton parameters over an interval that extends from 00:00 UT on August 3 to 00:00 UT on August 6. The bottom panel illustrates geomagnetic indices over the same interval. A detailed analysis of the near-Earth response to the series of CMEs launched on August 1 is provided by C. Möstl et al. (2012, in preparation) and Liu et al. (2012); here we endeavor to relate the CME speeds and 1 AU arrival times derived from visible-light imaging to the in situ measurements to see if such a comparison is found to be meaningful.

A point to note here is that the 1 AU arrival times and radial speeds quoted in previous sections are for the CME apex. For results based on application of the HM model, specifically, a geometrical correction must be applied for off-apex directions (Möstl et al. 2011). For the HM model, this correction is straightforward as the curvature of the transient front is defined by the model geometry. For any of the aforementioned CMEs that are propagating along a direction that is not closely aligned along the Sun–Earth line, we have implemented such a correction to derive arrival time and speed at Earth (arrival times are invariably later and speeds invariably slower for off-apex directions). Such a correction is not applicable for the FP model, in which the transient is assumed to be point-like in nature along the line of sight.

After its apparent interaction with L, no discernible features relating to CME M can be identified. This being so, it becomes hard to associate M with any in situ signatures because of the large gap between its loss in the visible-light observations and its expected arrival time at *Wind*, assuming a trajectory that impacts Earth. We leave M aside in the following discussion, although we note that we cannot definitively exclude the possibility that M is connected to one of the interplanetary CME structures seen by *Wind*. Some remnants of this feature may become apparent with more detailed analysis of the in situ signatures.

We conclude from our analysis, documented in Section 2.2.2, that CME L is likely propagating close to the Sun–Earth line, which would strongly suggest an impact at Earth. This being so, we can actually make an approximate estimate of the arrival of L at Earth based simply on the time at which the CME track crosses Earth's elongation of about noon on 2010 August 3 (within an observational limitation due to the HI-2 image cadence of 2 hr). If, rather more rigorously, we calculate an average arrival time at Earth based on all of the results presented in Section 2.2.2 (implementing, where necessary, a correction to account for the difference in longitude between the CME apex and the Earth for an HM model geometry), CME L is estimated to impact Earth at 13:30 UT on August 3 (vertical red dashed line in Figure 14); individual arrival times range from 10:00 to 17:00 UT on that day.

Figure 14 reveals the arrival of a shock at the *Wind* spacecraft at 17:05 UT on August 3 (labeled S2), which is within 4 hr of the predicted Earth-arrival time of CME L. Thus, we can associate this shock and the ensuing high-density sheath region with L. Shock arrival is characterized by an increase in solar wind speed from about 400 to 600 km s^{-1}, accompanied by an increase in total field strength, and proton temperature and density; the latter increases gradually in the sheath region to a maximum near 12 cm^{-3}. The magnetic field structure within the sheath is complex, exhibiting significant variation in both strength and direction. A particularly persistent southward magnetic field component (negative B_z) within the sheath region drives the first phase of the geomagnetic storm, which can be classified as either "moderate" based on a minimum Dst value of −77 nT or "strong" on the NOAA scale based on a maximum three-hourly Kp index of 7 (21:00 to 24:00 UT on August 3; see the bottom panel of Figure 14). Note that when magnetopause currents are taken into account the corrected Dst is just −100 nT, making this a borderline "major" storm.
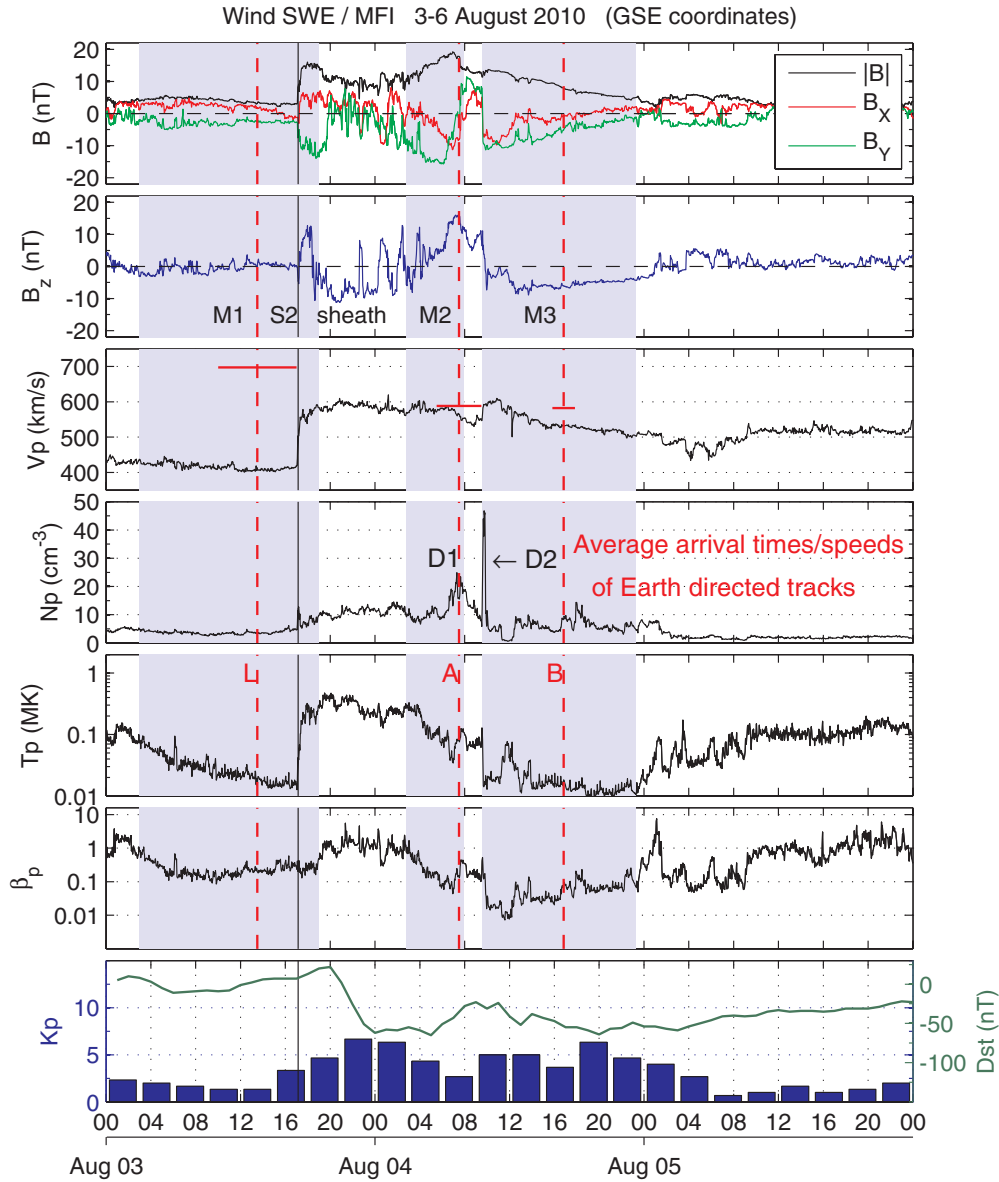
Figure 14. Magnetic field and solar wind proton bulk parameters observed by *Wind* with 2 minute time resolution during the interval 2010 August 3 00:00 UT to 2010 August 6 00:00 UT. The top panel presents total magnetic field strength (black) and the magnetic field X and Y components in Geocentric Solar Ecliptic (GSE) coordinates, B_x in red and B_y in green. The second panel presents B_z (GSE) in blue. The third, fourth, fifth, and sixth panels present proton speed, proton density, proton temperature, and proton beta, respectively (the latter being the ratio of plasma to magnetic pressure). The bottom panel presents the geomagnetic Kp (blue histogram) and Dst indices (green). A black vertical line on each panel marks the shock arrival at 17:05 UT on August 3. Shaded regions M1 to M3 demark magnetic flux ropes. Dashed red vertical lines correspond to the predicted arrival times of CMEs L, A, and B; solid red horizontal lines indicate both the uncertainty in this timing estimate and the estimated CME speed. D1 marks a density enhancement at the rear of M2 and D2, possibly filament material (C. Möstl et al. 2012, in preparation).

From the analysis presented in Section 2.2.3, we deduce that the FPF and HMF techniques are appropriate for CME A. For this CME, we estimate Earth-arrival times of 05:50 and 09:42 UT on August 4 for FPF and HMF, respectively. While the former is exactly as quoted in Table 2, the latter has, again, been corrected for the longitude difference between the fitted CME apex and Earth. In Figure 14, we plot an average arrival time for CME A of 07:30 UT ± 2 hr. Propagation directions of W4° (FPF) and E19° (HMF) suggest that CME A should impact Earth, and this we associate with a density enhancement (labeled D1 in Figure 14) detected at the rear of magnetic flux rope M2 ("flux ropes" are defined through a smooth rotation of the magnetic field vector over a large angle accompanied by a stronger-than-average total field strength). M2 is characterized

by a B_z reversal from south to north, which causes a short-lived recovery of the geomagnetic indices.

Similarly, for CME B we consider use of the FPF and HMF techniques valid (Section 2.2.4). Propagation directions of W9° and E12° derived from FPF and MHF analysis, respectively, suggest probable Earth impact. For CME B, we estimate Earth-arrival times of 15:49 and 17:41 UT on August 4 for FPF and HMF techniques, respectively (again with the latter corrected for the longitude of Earth), yielding an average arrival time of 16:50 UT ± 1 hr on August 4 (again marked in Figure 14). The obvious association is flux rope M3, characterized additionally by a very low proton temperature, consistent with the definition of a magnetic cloud (Burlaga et al. 1981). The consistently southward field within M3 again results in an enhancement in

geomagnetic activity that is comparable, in terms of its Kp and Dst response, to the one caused by the sheath region of CME L.

Horizontal red bars in the third panel of Figure 14 indicate the predicted radial speeds derived for L, A, and B. These are, again, average values of the results that are considered appropriate (as discussed for each CME earlier in this section). As before, any speeds resulting from the implementation of an HM-type geometry are corrected where Earth is off CME-apex. The average Earth-directed speeds are 697, 588, and 592 km s^{-1} for CME L, A, and B, respectively. These speeds are consistent with those of the in situ features with which they are identified as being associated.

There are some additional inferences that can be drawn from the in situ measurements. On the morning of August 3, the *Wind* spacecraft encounters a structure, labeled M1, which can be classified as a magnetic flux rope, with a very low proton temperature, most likely with a solar origin prior to August 1. Moreover, the fact that structure M2 exhibits high temperature and density, as well as an elevated field strength, could be a sign of interaction with M3 (Farrugia & Berdichevsky 2004). These features are discussed in detail by Liu et al. (2012).

The Earth-arrival times and speeds of the CMEs derived from the analysis of images from HI, an instrument that detects the electron density signatures of heliospheric transients, appear consistent with what is observed in situ near-Earth in plasma and magnetic field measurements, although the relationship is far from simple. The shock (S2) and the subsequent sheath region clearly correspond to the front of CME L, the arrival of CME A is consistent with a density enhancement (D1) at the rear of M2, and the arrival of CME B appears to be associated with a weak density enhancement in the center of M3. There is a large but short-lived density enhancement, D2, to the front of M3, which is shown by C. Möstl et al. (2012, in preparation) to comprise possible filament material. However, because it is of limited duration and proximity to D1, it is unlikely to be discernible as a discrete signature in the HI images.

3. CONCLUSIONS AND DISCUSSION

A series of four major near-Earth directed CMEs were launched between 02:00 and 18:00 UT on 2010 August 1. We have examined the kinematic properties of each CME using a number of established techniques, and also by use of a novel approach that was especially valuable for analyzing the fastest event that exhibited rapid deceleration from an initial speed in excess of 1000 km s^{-1}. Having established a range of possible solutions in terms of radial speed, propagation direction, launch time, and 1 AU arrival time, we have identified what we consider the most appropriate near-Sun and near-Earth associations for each CME. The principal conclusions are summarized as follows:

1. Despite the complexity of this period of activity, with four CMEs ejected in quick succession, we have demonstrated the capability to perform robust analysis of individual events. While we have applied the often-used FPF and HMF techniques to analyze three of these events, we stress, in particular, the value of the novel "fixed direction/variable speed" approach for analyzing CMEs that undergo rapid acceleration/deceleration such as the CME we label L.

2. The first CME, which we called M, was ejected at around 02:42 UT with a speed of some 732 km s^{-1}. Although launched from a location near E12°, this CME appeared to experience an eastward rotation close to the Sun to a longi-

tude of around E30°. CME M was obscured by the subsequent faster CME, L, as it approached an elongation of 12°, after which M was indistinguishable as a separate entity. Evidence suggests that an interaction between the two CMEs resulted in the slower event being subsumed. Examination of combined EUV, coronagraph, and heliospheric imaging data—the former from *STEREO* and *SDO*—reveals an intimate association between the launch of CME M and the eruption of prominence Fl$_0$, centered at E10° and somewhat north of the ecliptic. The event was followed by some minor B-class flaring.

3. CME L, which exhibited an intense signature in visible-light observations, had accelerated to a speed in excess of 1000 km s^{-1} prior to entering the HI field of view. Analysis suggests an ensuing period of rapid deceleration, which appears to coincide with its interaction with CME M, followed by modest deceleration to 1 AU and beyond. Results from FPF and HMF techniques indicate a propagation direction for CME L that is east of the Sun–Earth line, while fixed direction/variable speed analysis, which is considered more appropriate in this case, suggests that it is propagating west of the central meridian. Nevertheless, CME L appears to be closely associated with a C3.2 flare at E36°, although the CME is well into the coronagraph fields of view at the time of flare onset and peak. We associate CME L with the arrival of a distinct shock at Earth, at 17:05 UT on 2010 August 3.

4. Subsequently launched was CME A, a narrow loop-like CME that appears to contain the erupting material of filament FI$_1$. Analysis suggests that it is propagating at a speed of around 600 km s^{-1} along a longitude close to the Sun–Earth line but is directed significantly north of the ecliptic plane. CME A appears to be associated with a flux rope that arrives at Earth on 2010 August 4.

5. The final CME that we consider, CME B, seems to be closely associated with the eruption of the large prominence, FI$_3$. This CME propagates in a direction near to central meridian at a speed of between 560 and 610 km s^{-1} and appears to be associated with a magnetic cloud that arrives at Earth on 2010 August 4.

Thus, of the four major CMEs launched in rapid succession on August 1, three are closely associated with prominence eruptions, with only minor B-class flare activity in the complex set of active regions to the east of the filament channels. The other CME, associated with a C3.2 flare, is by far the fastest of the four CME events and is actually well underway when the flare occurs. We also conclude that the flare site appears to be somewhat east of the center of that CME.

The kinematic parameters that have been derived for these four CMEs (namely, speed, direction, and timing information) are being used as input to a numerical MHD model to explore their propagation and interaction with a view to predicting signatures at Earth. This will be the subject of another paper (D. Odstrcil et al. 2012, in preparation). Moreover, the CME parameters derived at 1 AU are being used to perform a thorough analysis of the impacts of these events at Earth and at other solar system bodies (C. Möstl et al. 2012, in preparation).

The association between these CMEs and surface activity at the Sun stresses that the role of flares in the CME eruption process is marginal, in the sense that three of the events are primarily associated with prominence activity and the one event associated with a flare appears to be in progress before flare onset and peak; moreover, there is evidence that the source

of that CME is actually west of the flaring active region. We note that the results of this study, as well as the modeling work performed by Schrijver & Title (2011), clearly indicate that the CME eruptions are driven by magnetic configurations that have become unstable or lacking in equilibrium and are associated with structures much larger in scale than any single active region. Similar magnetic configurations, which cater for flare-CME asymmetries and include an appropriate range of scale sizes, have been described elsewhere (see, e.g., Harrison 1991, and references therein).

The interval under study stresses the need for a magnetic scenario that is far removed from any standard CME-flare model (such as the so-called CSHKP model, which is derived from models by Carmichael, Sturrock, Hirayama, Kopp, and Pneuman; see, e.g., Yashiro et al. 2008). These standard models call for a symmetry and coincidence in timing between the ascending CME structure and the underlying flare/active region activity that is not compatible with the August 1 observations. The flares associated with the August 1 sequence of CMEs are minor, occur after CME onset, and are located in the active region system that lies to the side of the principal region of CME eruption. The scale sizes of the CMEs suggest that their source regions are much larger than individual active regions. However, all of these observations are consistent with the CME scenarios reviewed by Harrison (1991, 2009). In fact, this sequence appears to be a classic case of large-scale magnetic complexity resulting in a variety of responses over a number of interconnected regions, including prominence channels and active regions, and culminating in a sequence of associated eruptions and explosions.

On the heliospheric side, the emphasis of this work has been on the arrival of these CMEs at Earth. We note that the Thomson surface for the *STEREO-A* spacecraft location at the time of these observations preferentially favors the observation of CMEs propagating west of the Sun–Earth line, whereas in situ observations show that CME flows east of the Sun–Earth line were actually faster and associated with stronger total magnetic field strength than those observed at Earth (C. Möstl et al. 2012, in preparation). In addition, analysis and interpretation of density and velocity observations reconstructed on the basis of interplanetary scintillation data from the Ootacamund (Ooty) Radio Telescope (ORT) will be carried out for this interval as per Bisi et al. (2009); this, again, will be the subject of a forthcoming paper.

Finally, we note that during this interval the *STEREO* spacecraft were within 20° of the L4 and L5 Lagrangian points (60° separation from Earth). These locations are often suggested to be key in terms of future space weather monitoring missions. Even at almost 80° separation from Earth, as in the case of *STEREO-A*, we are easily able to identify Earth-directed CMEs and provide robust predictions of their 1 AU arrival times. However, given that the current analysis incorporates not only the Sun–Earth line coronal and heliospheric imaging, but also near-Earth instrumentation—that provided us with in situ and EUV imaging—it is clear that a multi-platform capability is critical.

REFERENCES

Acũna, M. H., Ogilvie, K. W., Baker, D. N., et al. 1995, Space Sci. Rev., 71, 207
Bale, S. D., Ullrich, R., Goetz, K., Alster, N., & Cecconi, B. 2008, Space Sci. Rev., 136, 529
Bisi, M. M., Jackson, B. V., Clover, J. M., et al. 2009, Ann. Geophys., 27, 4479
Bisi, M. M., Jackson, B. V., Hick, P. P., et al. 2008, J. Geophys. Res., 113, A00A11
Bothmer, V., & Schwenn, R. 1998, Ann. Geophys., 16, 1
Bougeret, J.-L., Goetz, K., Kaiser, M. L., et al. 2008, Space Sci. Rev., 136, 487
Brueckner, G. E., Howard, R. A., Koomen, M. J., et al. 1995, Sol. Phys., 162, 357
Burlaga, L. F., Sittler, E., Mariani, F., & Schwenn, R. 1981, J. Geophys. Res., 86, 6673
Cargill, P. J. 2004, Sol. Phys., 221, 135
Cremades, H., & Bothmer, V. 2004, A&A, 422, 307
Davies, J. A., Harrison, R. A., Rouillard, A. P., et al. 2009, Geophys. Res. Lett., 36, L02102
de Koning, C. A., & Pizzo, V. J. 2011, Space Weather, 9, S03001
Eyles, C. J., Harrison, R. A., Davis, C. J., et al. 2009, Sol. Phys., 254, 387
Eyles, C. J., Simnett, G. M., Cooke, M. P., et al. 2003, Sol. Phys., 217, 319
Farrugia, C. J., & Berdichevsky, D. B. 2004, Ann. Geophys., 22, 3679
Gopalswamy, N. 2004a, in The Sun and the Heliosphere as an Integrated System, ed. G. Poletto & S. Suess (Dordrecht: Kluwer), 201
Gopalswamy, N. 2004b, Planet. Space Sci., 52, 1399
Gopalswamy, N., Tashiro, S., Kaiser, M. L., & Howard, R. A. 2003, Adv. Space Res., 32, 2613
Gopalswamy, N., Yashiro, S., Kaiser, M. L., Howard, R. A., & Bougeret, J.-L. 2001, ApJ, 548, L91
Gopalswamy, N., Yashiro, S., Michałek, G., et al. 2002, ApJ, 572, L103
Harrison, R. A. 1991, Phil. Trans. R. Soc. A, 336, 401
Harrison, R. A. 1995, A&A, 304, 585
Harrison, R. A. 2009, in Proc. IAU Symp. 257, Universal Heliophysical Processes, ed. N. Gopalswamy & D. F. Webb (Cambridge: Cambridge Univ. Press), 191
Harrison, R. A., Davis, C. J., Eyles, C. J., et al. 2008, Sol. Phys., 247, 171
Howard, R. A., Moses, J. D., Vourlidas, A., et al. 2008, Space Sci. Rev., 136, 67
Jackson, B.V., Buffington, A., Hick, P. P., et al. 2004, Sol. Phys., 255, 177
Jackson, B.V., Buffington, A., Hick, P. P., et al. 2010a, ApJ, 724, 829
Jackson, B. V., Hick, P. P., Buffington, A., et al. 2010b, in Proc. 6th Asia-Oceania Geophysical Society General Assembly, Advances in Geosciences, Vol. 21: Solar & Terrestrial Science (2008), ed. M. Duldig (Singapore: World Scientific), 339
Jackson, B.V., Hick, P. P., Buffington, A., et al. 2011, J. Atmos. Sol.–Terr. Phys., 73, 1214
Kaiser, M. L., Kucera, T. A., Davila, J. M., et al. 2008, Space Sci. Rev., 136, 5

Leblanc, Y., Dulk, G. A., & Bougeret, J.-L. 1998, Sol. Phys., 183, 165
Lepping, R. P., Acūna, M. H., Burlaga, L. F., et al. 1995, Space Sci. Rev., 71, 207
Liu, Y., Davies, J. A., Luhmann, J. G., et al. 2010a, ApJ, 710, L82
Liu, Y., Luhmann, J. G., Bale, S. D., & Lin, R. P. 2009, ApJ, 691, L151
Liu, Y., Luhmann, J. G., Moestl, C., et al. 2012, ApJ, 746, L15
Liu, Y., Thernisien, A., Luhmann, J. G., et al. 2010b, ApJ, 722, 1762
Lugaz, N. 2010, Sol. Phys., 267, 411
Lugaz, N., Hernandez-Charpak, J. N., Roussev, I. I., et al. 2010, ApJ, 715, 493
Martinez Oliveros, J. C., Raftery, C. L., Bain, H. M., et al. 2012, ApJ, 748, 66
Möstl, C., Rollett, T., Lugaz, N., et al. 2011, ApJ, 734, 34
Möstl, C., Temmer, M., Rollett, T., et al. 2010, Geophys. Res. Lett., 37, L24103

Ogilvie, K. W., Chornay, D. J., Fritzenreiter, R. J., et al. 1995, Space Sci. Rev., 71, 55
Rollett, T., Möstl, C., Temmer, M., et al. 2012, Sol. Phys., 276, 293
Rouillard, A. P., Davies, J. A., Forsyth, R. J., et al. 2008, Geophys. Res. Lett., 35, L10110
Rouillard, A. P., Savani, N., Davies, J. A., et al. 2009, Sol. Phys., 256, 307
Schrijver, C., & Title, A. 2011, J. Geophys. Res., 116, A04108
Sheeley, N. R., Herbst, A. D., Palatchi, C. A., et al. 2008, ApJ, 675, 853
Sheeley, N. R., Walters, J. H., Wang, Y.-M., & Howard, R. A. 1999, J. Geophys. Res., 104, 24739
Temmer, M., Vršnak, B., Rollett, T., et al. 2012, ApJ, 749, 57
Webb, D. F., Möstl, C., Jackson, B. V., et al. 2012, Sol. Phys., submitted
Yashiro, S., Michalek, G., Akiyama, S., Gopalswamy, N., & Howard, R. A. 2008, ApJ, 673, 1174